Development of a multi-way coupled discrete-finite element method simulation procedure for modelling soil-passive vibration tool interaction

László Pásthy [a], Zsolt József Farkas [a], Tamás Haba [b], Kornél Tamás [a,*]

[a] Department of Machine and Product Design, Faculty of Mechanical Engineering, Budapest University of Technology and Economics, Műegyetem rkp. 3, H-1111 Budapest, Hungary
[b] Department of Mechatronics, Optics and Mechanical Engineering Informatics, Faculty of Mechanical Engineering, Budapest University of Technology and Economics, Műegyetem rkp. 3, H-1111 Budapest, Hungary

ABSTRACT

Among the energy-saving tillage solutions, a promising technology is the application of passive vibration-based soil tillage tools. If the appropriate tillage parameters are applied, a tillage tool which involves vibration-based motion can reduce the draught force and energy requirements of the tillage process while enhancing its quality. The main focus of our research was on developing a coupled discrete-finite element procedure to investigate the interaction between passively vibrating tools and the soil. To validate this method, a soil bin measuring system was constructed to investigate the operation of a highly rigid structural steel (S235) tool along with a more flexible polymethyl methacrylate (PMMA) tool, with the soil bin at working depths of 18, 30, and 42 mm, tool velocities between 28 and 37 mm s^{-1}, in sandy soil with 1 ± 0.1 % dry based moisture content. Soil bin measurements with the highly rigid S235 tool were simulated using the discrete element method (DEM) along with a coupled discrete-finite element (DEM-FEM) procedure, while the soil bin measurements applying the more flexible PMMA tool were simulated using the coupled DEM-FEM procedure. In the case of DEM calculations the hysteretic spring and linear cohesion contact models were applied, and in the case of FEM calculations the transient, linear elastic model was utilised with Rayleigh damping. During the parameter calibration process it was observed that the soil properties depend on depth, therefore a multi-layered soil model was created. After parameter calibration the simulated mean force and deformation values matched the measured values with less than 15 % difference. Furthermore the simulation results also supported the assumption that passively vibrating tillage tools loosen and mix the soil more effectively. Based on these results, it can be concluded that the coupled DEM-FEM procedure enabled the accurate modelling of passively vibrating tillage tools.

1. Introduction

In the present day, due to the increasing world population and ever more frequent food crises, there is a growing interest in sustainability in the agricultural industry. One possible way to achieve sustainability and increase the energy efficiency of agricultural processes is the utilisation of vibrating sweep tools (Dzhabborov et al., 2021), vibrating harrows (Upadhyay and Raheman, 2020; Usaborisut et al., 2020) and vibrating subsoilers (Van der Linde, 2007; Wang et al., 2020) in the soil loosening and pulverization processes. These tools can be divided into two broad categories: actively and passively vibrating tools. While actively vibrating tools require additional energy input, which increases their cost of operation, passively vibrating tools do not require such energy

input, as they produce a vibratory motion in the soil due to their elastic suspension and the variable levels of soil resistance caused by soil inhomogeneity. Both actively vibrating tools (Rao et al., 2018; Wang et al., 2020) and passively vibrating tools (Keppler et al., 2015; Fenyvesi and Hudoba, 2010; Dzhabborov et al., 2021) reduce the amount of draught force required to till the soil and improve the tillage quality compared to rigidly suspended tools. This phenomenon was first proven empirically by Gunn and Tramontini (1955), and has since continued to be a subject of research.

Analytical formulas have been developed to describe the interaction between vibrating tillage tools and the soil. The calculation of the draught force requirement for actively vibrated tools was first formulated by Kofoed (1969). To describe the motion of passively vibrating tools, Fenyvesi and Hudoba (2010) derived equations using the

---

Nomenclature

General parameters

m	mass of calibration weight (kg)
Δx	displacement in the x direction (m)
Δy	displacement in the y direction (m)
Δz	displacement in the z direction (m)

DEM micromechanical parameters

D	particle diameter (mm)
$\rho_{particle}$	particle density (kg m^{-3})
$E_{particle}$	Young's modulus of the particles (Pa)
$G_{particle}$	shear modulus of the particles (Pa)
$\nu_{particle}$	Poisson's ratio of the particles (–)
Y	yield strength of the particles (Pa)
$\rho_{DEMPMMA}$	density of the PMMA tool in the DEM simulation (kg m^{-3})
$E_{DEMPMMA}$	Young's modulus of the PMMA tool in the DEM simulation (Pa)
$G_{DEMPMMA}$	shear modulus of the PMMA tool (Pa)
$\nu_{DEMPMMA}$	Poisson's ratio of the PMMA tool in the DEM simulation (–)
$\rho_{DEMsteel}$	density of the soil bin and the S235 tool in the DEM simulation (kg m^{-3})
$E_{DEMsteel}$	Young's modulus of the soil bin and the S235 tool in the DEM simulation (Pa)
$G_{DEMsteel}$	shear modulus of the soil bin and the S235 tool (Pa)
$\nu_{DEMsteel}$	Poisson's ratio of the soil bin and the S235 tool in the DEM simulation (–)
e_{pp}	coefficient of restitution between particles (–)
μ_{pp}	rolling friction coefficient between particles (–)
μ_{0pp}	static friction coefficient between particles (–)
γ_t	stiffness factor between particles (–)
b_n	damping factor between particles (–)
K	cohesion energy density between particles (J m^{-3})
e_{sp}	coefficient of restitution between particles and the soil bin and between particles and the soil-engaging tools (–)
μ_{sp}	rolling friction coefficient between particles and the soil bin and between particles and the soil-engaging tools (–)
μ_{0sp}	static friction coefficient between particles and the soil bin and between particles and the soil-engaging tools (–)
Δt_{DEM}	time step in the DEM simulation (s)

FEM macromechanical parameters

$\mathbf{f}_i$	force vector in the time step i (N)
$\mathbf{u}_i$	displacement vector in the time step i (m)
$\mathbf{M}$	mass matrix
$\mathbf{C}$	damping matrix
$\mathbf{K}$	stiffness matrix
$\ddot{\mathbf{U}}$	acceleration vector (m s^{-2})
$\dot{\mathbf{u}}$	velocity vector (m s^{-1})

|	
$\mathbf{U}$	displacement vector (m)
α_{PMMA}	Rayleigh damping component of the PMMA tool proportional to the stiffness matrix (–)
β_{PMMA}	Rayleigh damping component of the PMMA tool proportional to the mass matrix (–)
$E_{FEMPMMA}$	Young's modulus of the PMMA tool in the FEM simulation (Pa)
$\nu_{FEMPMMA}$	Poisson's ratio of the PMMA tool in the FEM simulation (–)
$\rho_{FEMPMMA}$	density of the PMMA tool in the FEM simulation (kg m^{-3})
α_{steel}	Rayleigh damping component of the S235 tool proportional to the stiffness matrix (–)
β_{steel}	Rayleigh damping component of the S235 tool proportional to the mass matrix (–)
$E_{FEMsteel}$	Young's modulus of the soil bin and the S235 tool in the FEM simulation (Pa)
$\nu_{FEMsteel}$	Poisson's ratio of the soil bin and the S235 tool in the FEM simulation (–)
$\rho_{FEMsteel}$	density of the soil bin and the S235 tool in the FEM simulation (kg m^{-3})
$\mathbf{A}_1$	coefficient matrix of the displacement vector in the FEM fundamental equation in the time step i + 1
$\mathbf{A}_2$	coefficient matrix of the displacement vector in the FEM fundamental equation in the time step i
$\mathbf{A}_3$	coefficient matrix of the displacement vector in the FEM fundamental equation in the time step i − 1
$\mathbf{K}_{aa}$	submatrix of the stiffness matrix which does not depend on the keypoints
$\mathbf{K}_{bb}$	submatrix of the stiffness matrix which only depends on the keypoints
$\mathbf{K}_{ab}, \mathbf{K}_{ba}$	submatrices of the stiffness matrix which depend on the keypoints and on other nodes too
$\mathbf{u}_a$	subvector of the displacement vector consisting of keypoints (m)
$\mathbf{u}_b$	subvector of the displacement vector consisting of nodes which are not keypoints (m)
$\mathbf{f}_a$	subvector of the force vector consisting of keypoints (m)
$\mathbf{f}_b$	subvector of the force vector consisting of nodes which are not keypoints (m)
Δt_{FEM}	time step in the FEM simulation (s)

Abbreviations

DEM	Discrete Element Method
FEM	Finite Element Method
S235	Structural steel with 235 MPa yield strength
PMMA	Polymethyl methacrylate
CPR	Cone Penetration Resistance
FFT	Fast Fourier Transform

Lagrange equation. However, these analytical formulas are limited in their applicability and can only be used in specific cases, and even in these cases, they do not provide information about changes in soil quality or about tool deformation.

Numerous studies have been conducted on actively vibrating tillage tools. Van der Linde (2007) focused on investigating a vibratory subsoiler. He conducted measurements and performed discrete element method (DEM) simulations, although the results of the simulation and the results from empirical measurement showed only qualitative agreement without finding a precise quantitative correspondence. Wang et al., (2018) created an electro-hydraulic control system for a flexible-tine subsoiler and demonstrated through field measurements that the

system thus developed was able to improve the quality of soil cultivation. Wang et al., (2020) subsequently confirmed through field measurements that the control system they developed for a vibrating subsoiler requires less draught force and can achieve less wheel slippage compared to passive tool suspension, while the power requirement for the controlled and passive tool suspension systems was roughly similar. Upadhyay and Raheman (2020) took measurements to compare a partially actively vibrated compact disc harrow configuration and a conventional passive compact disc harrow. The vibrated disc harrow produced a more uniform tillage depth, better soil pulverization capability, lower traction force, and reduced wheel slippage although its fuel and energy consumption increased compared to the conventional disc
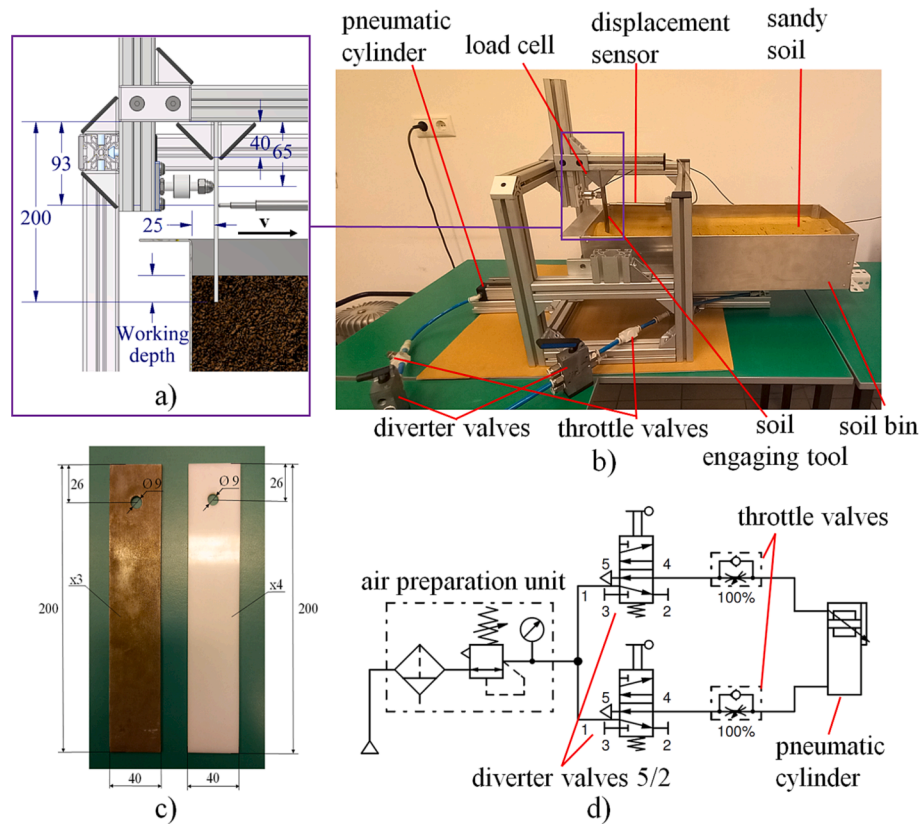
Fig. 1. Measurement setup in the initial state: (a) clamping dimensions of the soil-engaging tool, (b) soil bin measurement system, (c) dimensions of the S235 (left) and PMMA (right) tool, (d) schematic diagram of the pneumatic system (dimensions are given in mm, and the relative movement direction of the soil-engaging tools is denoted by the vector **v**).

harrow.

Passively vibrating tillage tools are mostly applied when there is a relatively great draught force requirement, for the purpose of draught force reduction. In contrast to actively vibrating tillage tools, the topic of passively vibrating tillage tools remains relatively unexplored, with limited research conducted and a relative dearth of related literature. Based on our review of the literature, only Zhang (1997), Fenyvesi and Hudoba (2010), Keppler et al. (2015) and Dzhabborov et al. (2021) have conducted experiments with passively vibrating tillage tools.

In addition to analytical formulas, another option for describing soil tillage is the application of numerical simulations, which are more cost-effective and less time-consuming than taking measurements, and more widely applicable than analytical formulas. Among the numerical simulations applied, the most commonly used method for modelling soil-tool interaction, along with the finite element method (FEM) (Ben-taher et al., 2013; Naderi-Boldaji et al., 2013), is the DEM. Numerous researchers have used this method to investigate various soil tillage processes (Keppler et al., 2015; Ucgul et al., 2015; Tamás and Bernon, 2021). However, in the aforementioned studies, the deformation of the tool upon contact with the soil was not considered, as the DEM itself can only handle rigid geometries. The forces acting on the geometry can be obtained and taken into consideration, but the shape of the geometry generally does not change during a DEM simulation. Since in reality the deformation of the tool is often significant and cannot be neglected, ignoring it in simulations leads to inaccuracies.

The DEM has also been used in research into passively vibrating tools. In a comparative study using both soil bin measurements and DEM simulations Keppler et al. (2015) found an average reduction of 18 % in draught force required for the passively vibrating tillage tool compared to the rigid tool. However, their DEM model did not fully replicate reality, as the tool was actively vibrated in the DEM simulation. A solution

to this could be the application of two-way coupled DEM-FEM simulations, where the soil motion is modelled by the DEM, while the tool's deformation is calculated by the FEM.

Two-way coupled DEM-FEM simulations have already been used to model soil-tyre interaction. Michael et al. (2015) utilized a DEM-FEM simulation procedure they developed to model the deformation of a rolling and sliding rubber tyre on soil. They took into consideration external forces arising from the tyre-soil interaction and the internal tyre pressure. For spatial approximation in the finite element method, they employed the Galerkin method, and for temporal discretization, they used a central difference scheme. Nishiyama et al. (2018) developed a two-dimensional DEM–FEM procedure capable of calculating the deformation of rubber tyres rolling on the ground. They modelled the soil using a finite element mesh further away from the tyre, while closer to the tyre they automatically converted the elements into discrete particles. Yang et al. (2020) validated their DEM-FEM simulation procedure developed for modelling the deformation of rubber tyres by taking field measurements in gravelly soil. Zeng et al. (2020) developed a calibration procedure to determine the parameters of a DEM-FEM model of soil-tyre interaction. They validated the calibration procedure thus developed via field measurements using sandy soil. In general, studies modelling soil-tyre interaction have found that the maximum specific elongation of tyres is typically only 3–5 %, which did not result in visually perceptible deformations.

To date, however, based on our review of the literature, there have been no examples of the application of two-way coupled DEM-FEM simulations to soil-tillage tool interaction. This method provides an opportunity to model passively vibrating tillage tools more accurately, as it allows the transient vibrations of the tool caused by the excitation effect of the soil on the tool to be taken into consideration. Currently, however, no commercial or open-source software is available for this

purpose, so the development of customised software would be necessary.

Based on the identified shortcomings in the literature, our research aims to accomplish the following tasks: (1) To develop a two-way coupled DEM-FEM simulation procedure that can be applied to model the interaction between deformable tillage tools and the soil, as well as modelling the passive vibration of tillage tools in the soil. (2) To create a measurement system for laboratory experiments that is suitable for validating the coupled DEM-FEM simulation procedure developed in point (1). (3) To calibrate the simulation parameters using laboratory measurements. (4) To perform additional two-way coupled DEM-FEM simulations and compare the results with the laboratory measurements in terms of both their qualitative and quantitative aspects. Specifically, to investigate the forces acting on the tool, along with the deformation characteristics, and vibration properties of the tool. (5) To analyse the movement and mixing of soil particles in the simulations. By accomplishing these tasks, we aim to contribute to the understanding and accurate modelling of soil-tool interactions and the behaviour of passively vibrating tillage tools.

2. Materials and methods

2.1. Measurement system

A soil bin measurement system (Fig. 1a) was built to evaluate the applicability of the coupled simulation procedure developed by the authors. This apparatus allows us to measure the forces acting on a horizontally drawn simple soil-engaging tool, as well as the levels of deformation and vibration of the tool. The 650 mm long, 250 mm wide, 150 mm high soil bin is moved by a pneumatic, mechanically jointed, rodless cylinder with a 600 mm stroke (Fig. 1d). Levelling elements can be placed under the soil bin to enable it to be tested at three different working depths (18 mm, 30 mm and 42 mm). The soil-engaging tool is clamped to the frame structure at its upper end with a 40 mm offset (Fig. 1a), and the forces acting on it are determined using a load cell (U9B, Hottinger Baldwin Messtechnik GmbH, Germany) which is located 65 mm directly beneath the top of the tool (Fig. 1a). The displacement of the tool is measured by means of a contact-type displacement sensor (WTK10, Hottinger Baldwin Messtechnik GmbH, Germany) located 93 mm beneath the top of the tool. The pneumatic system (Fig. 1d) consists of two throttle valves, two 5/2-way valves, and a mechanically-jointed rodless cylinder. The 5/2-way valves control the initiation and termination of the cylinder's movement, while the consistent velocity of the cylinder is ensured by the 6 bar supply pressure of the system and the secondary throttle valves, which allow the cylinders to approach the system's maximum pressure, so the system can be operated with maximum rigidity. Furthermore, the consistency of the velocity was verified visually, as no significant velocity fluctuations were observed in the video recordings of the individual measurements (available online as additional material). However, because the throttle valves were kept at the same setting, and the magnitude of the forces acting on the tool varied at different working depths, the average velocity of the tool was not the same at all three working depths, but varied between 28 and 37 mm s^{-1}. The data from the load cell and the displacement sensor was collected parallelly at a frequency of 50 Hz using an electronic data acquisition system (Spider 8, Hottinger Baldwin Messtechnik GmbH, Germany).

2.2. Granular material and test specimens

For the measurements, the same soil composition (93.28 % sand, 4.66 % silt, 2.06 % clay) was used as in the research by Tamás (2018). The dry basis moisture content of the sand was 1 ± 0.1 %, which was measured using an electrical moisture sensor (ML3 ThetaProbe, Delta-T Devices Ltd, United Kingdom).

The soil bin was filled with the sandy soil up to a height of 112 mm.

Before each measurement, the soil condition was rendered nearly identical for each occasion by loosening the sand with a shovel and manually shaking the soil bin, then smoothed down with a shovel to produce a virtually uniform soil surface.

The measurements were made using a 200 mm long, 40 mm wide, 3 mm thick S235JRG2 (S235) tool and a 200 mm long, 40 mm wide, 4 mm thick polymethyl-methacrylate (PMMA) tool. The soil-engaging tools (Fig. 1c) were inserted into the soil vertically to depths of 18, 30, and 42 mm. The velocity of the tools depended on the draught force applied but always fell within the range of 28–37 mm s^{-1} (Abo-Elnor et al., 2003). This velocity range proved to be suitable for ensuring a nearly steady-state condition, in which the force acting on the tool and the deformation of the tool oscillated around a nearly constant value, while the computational time for the simulations remained manageable. Each measurement was repeated 5 times.

2.3. Evaluation of data

The raw measurement data was processed using data evaluation software that was developed in-house, programmed in C# for the NET platform (Liberty, 2005). The first valuable data point was determined by performing a linear fit: the points at which the deformation first reached 10 % and 20 % of its maximum value were identified, and a straight line was plotted between these two points. Then the origin point of the data was shifted to the point where the fitted line intersected the initial deformation value, (Suhr and Six, 2017, Szabó et al., 2022). Since the force acting on the tool increased significantly at the end of the measurement due to the effects of the approaching wall, the end of the measurement was determined by finding the maximum of the measurement data, and the subsequent data points were eliminated. For each time point from the start of the measurement to the end, a tool displacement value was assigned, such that the displacement was 0 mm at the start of the measurement and the displacement was equal to the stroke length of the cylinder, i.e., 600 mm, at the end of the measurement. The displacement of the soil-engaging tool between these two points was divided evenly between the data points. Finally, the measured data was multiplied by the calibration factors determined using sensor calibration, resulting in the deformation values in mm and the force values in N.

Based on the measured data, the tool displacement-force and tool displacement-deformation curves were calculated and analysed. Additionally, the mean and standard deviation values were calculated in a range of 100–500 mm tool displacement at the 3 working depths utilised. Furthermore, in order to compare the characteristic vibration amplitudes and frequencies observed during the measurements and simulations, the results were converted to the frequency domain using Fast Fourier Transform (FFT), using the built-in algorithm of Microsoft Excel 2013® (Cho, 2018).

2.4. Coupled DEM-FEM simulation with EDEM coupling interface

For the DEM part of the simulations, Altair EDEM 2020® software was utilized. For the FEM part of the simulations, coupling client FEM software that had been developed in-house was utilized and connected to EDEM with EDEM Coupling Interface, which provides an application programming interface (API) for interacting with EDEM during coupled simulations (Programming Guide, n.d.). The API includes data structures and functions that allow direct intervention in the DEM simulation process. With respect to coupling, the following functions are crucial: *getAllLocalNodePositions* retrieves the positions of specific geometry nodes in the local coordinate system of the body, *getNodeForceVectors* retrieves the forces transmitted through specific geometry nodes, *setAllLocalNodePositions* repositions the nodes of a given geometry to specified positions in the local coordinate system of the geometry, and *simulate* starts the DEM simulation for a specified period of time. These functions allow the user to interact with the DEM simulation by
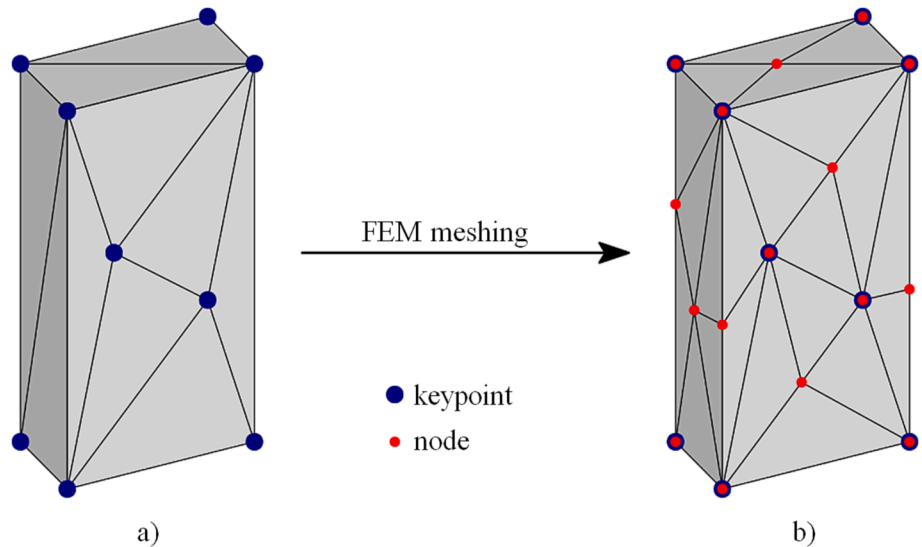
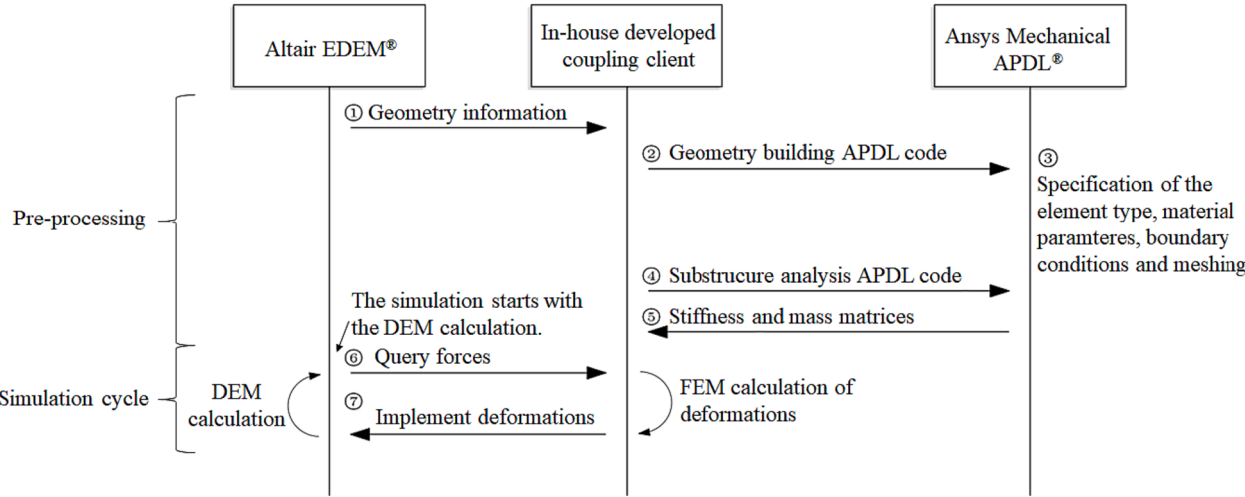**Fig. 2.** Relationship between (a) the DEM mesh and (b) the FEM mesh.

Fig. 3. Sequential diagram of the coupled DEM-FEM procedure.

Table 1
Required time of measurements and simulations.

	Working depth [mm]	Velocity [mm s^{-1}]	Measurement time [s]	Required computational time [h]	Proportion of DEM [%]	Proportion of FEM [%]
DEM simulation of the S235 tool	18	31.19	19.24	44	100	0
	30	30.03	19.98	46	100	0
	42	32.22	18.62	43	100	0
DEM-FEM simulation of the S235 tool	18	31.19	19.24	28	96.4	3.6
	30	30.03	19.98	52	96.5	3.5
	42	32.22	18.62	96	98.1	1.9
DEM-FEM simulation of the PMMA tool	18	36.14	16.60	46	96.5	3.5
	30	28.76	20.86	54	96.4	3.6
	42	34.09	17.60	42	96.4	3.6

retrieving node positions and forces, modifying node positions, and starting the simulation process.

A key feature enabling successful coupling is that the nodes of the mesh describing the soil-engaging tool's geometry can be repositioned during the simulation, allowing the tool to deform. The precise nature of this deformation can be calculated based on the forces acting on the tool using an appropriate solid mechanics model.

The DEM and FEM calculations are performed alternately in the simulation cycle illustrated in Fig. 3. The discrete element simulation determines how the positions of the particles have changed during a given time step (Δt_{DEM}), as well as the forces transferred from the particles to the soil-engaging tool. The task of the FEM simulation time step (Δt_{FEM}) is to determine the deformation of the tool for the next ($i + 1$) simulation step based on the forces acting on the tool and the deformations from the previous simulation steps:
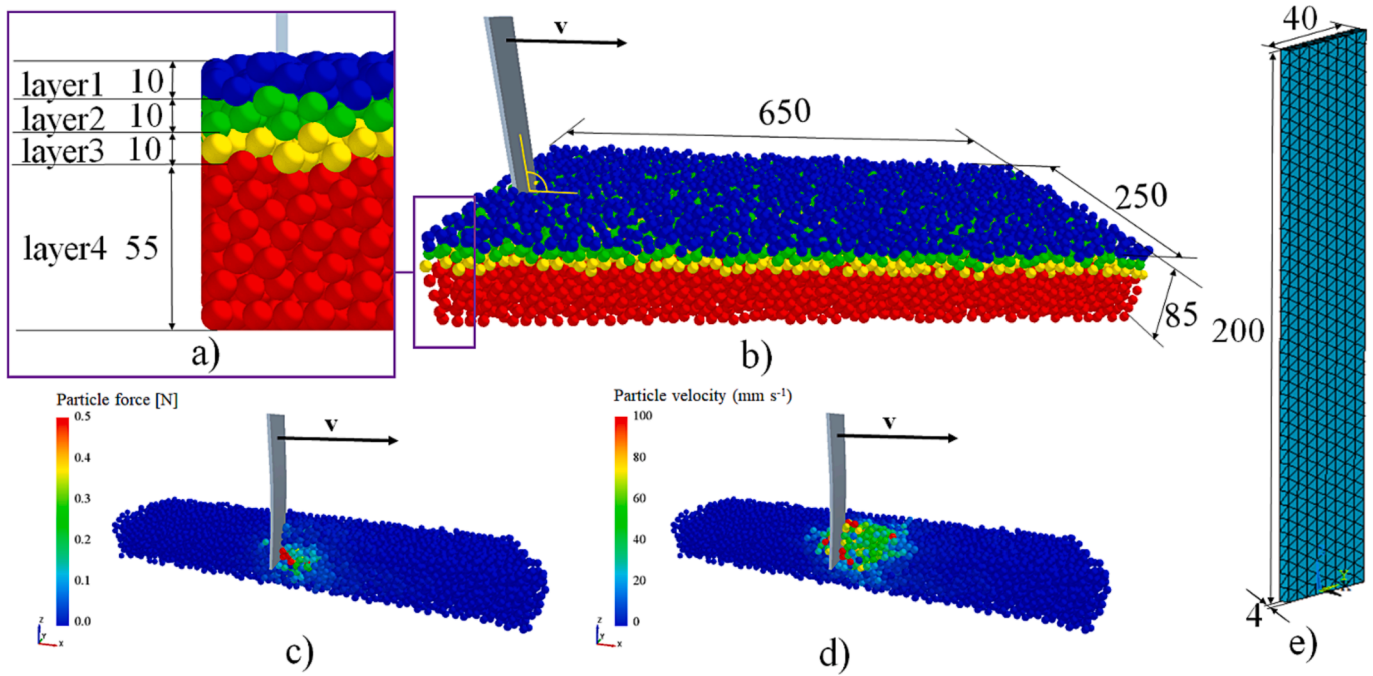
Fig. 4. Simulation model of the soil-passively vibrating tool interaction: (a) layers of the DEM assembly, (b) dimensions of the DEM assembly and initial position of the soil-engaging tool (the perpendicular angle of the tool to the surface of the particle assembly is marked with a yellow notation), (c) forces acting on particles and (d) particle velocities within the DEM assembly at the vertical cross-section of the assembly in the DEM-FEM simulation of the PMMA tool at a working depth of 42 mm and a tool displacement of 300 mm. (e) meshed geometry of the PMMA tool (the direction of tool velocity is indicated by vector **v**, dimensions are in mm). (For interpretation of the references to colour in this figure legend, the reader is referred to the web version of this article.)

$$(\mathbf{f}_i, \mathbf{f}_{i-1}, \cdots, \mathbf{u}_i, \mathbf{u}_{i-1}, \cdots) \mapsto \mathbf{u}_{i+1} \tag{1}$$

where $\mathbf{f}_i$ (N) is the force vector in time step i, and $\mathbf{u}_i$ (mm) is the displacement vector in time step i.

2.5. Finite element method

The deformation of the soil-engaging tool under a time-independent load can be determined using the static finite element method equation:

$$\mathbf{Ku} = \mathbf{f} \tag{2}$$

where **K** is the stiffness matrix, **u** is the displacement vector containing the displacements of the nodes of the FEM mesh and **f** is the force vector.

However, in DEM simulations, the forces acting on the soil-engaging tool are continuously changing, causing its degree of deformation to vary continuously. Therefore, instead of using the static finite element method equation, a dynamic finite element method equation was applied in order to determine the degree of deformation of the tool in the $i+1$ time step (Dongbao et al., 2021; Zhong et al., 2022):

$$\mathbf{M\ddot{u}} + \mathbf{C\dot{u}} + \mathbf{Ku} = \mathbf{f} \tag{3}$$

where $\mathbf{\ddot{u}}$ is the acceleration vector, $\mathbf{\dot{u}}$ is the velocity vector, **u** is the displacement vector, **f** is the nodal force vector, **M** is the mass matrix assembled based on the tool geometry and density, **K** is the stiffness matrix assembled based on the geometry and elasticity of the tool, and **C** is the damping matrix calculated using Rayleigh theory. This is similar to the approach followed by Dongbao et al. (2021):

$$\mathbf{C} = \alpha \bullet \mathbf{K} + \beta \bullet \mathbf{M} \tag{4}$$

The damping matrix consists of two components: one proportional to the stiffness matrix and one proportional to the mass matrix. The proportionality factor for the stiffness matrix is denoted as α, while the pro-

portionality factor for the mass matrix is denoted as β.

A third-order central finite difference scheme, similar to that used by Michael et al. (2015) was utilized to determine the relationship between nodal displacement, acceleration and velocity vectors over time. Applying this method, the dynamic finite element equation can be written in the following form:

$$\mathbf{M} \bullet \frac{1}{\Delta t^2}(\mathbf{u}_{i+1} - 2\mathbf{u}_i + \mathbf{u}_{i-1}) + \mathbf{C} \bullet \frac{1}{2\Delta t}(\mathbf{u}_{i+1} - \mathbf{u}_{i-1}) + \mathbf{K} \bullet \frac{1}{3}(\mathbf{u}_{i+1} + \mathbf{u}_i + \mathbf{u}_{i-1})$$
$$= \frac{1}{3}(\mathbf{f}_{i+1} + \mathbf{f}_i + \mathbf{f}_{i-1}) \tag{5}$$

To allow faster computation, the following constant terms can be extracted from the equation and calculated before starting the simulation:

$$\mathbf{A}_1 = \left(\frac{\mathbf{M}}{\Delta t^2} + \frac{\mathbf{C}}{2\Delta t} + \frac{\mathbf{K}}{3}\right) \tag{6}$$

$$\mathbf{A}_2 = \left(\frac{2\mathbf{M}}{\Delta t^2} - \frac{\mathbf{K}}{3}\right) \tag{7}$$

$$\mathbf{A}_3 = \left(-\frac{\mathbf{M}}{\Delta t^2} + \frac{\mathbf{C}}{2\Delta t} - \frac{\mathbf{K}}{3}\right) \tag{8}$$

Thus, the dynamic finite element equation becomes:

$$\mathbf{u}_{i+1} = \mathbf{A}_1^{-1}\left(\frac{1}{3}(\mathbf{f}_{i+1} + \mathbf{f}_i + \mathbf{f}_{i-1}) + \mathbf{A}_2 \bullet \mathbf{u}_i + \mathbf{A}_3 \bullet \mathbf{u}_{i-1}\right) \tag{9}$$

Rearranging the equation, the force vector in time step $i + 1$ can be obtained:

$$\mathbf{f}_{i+1} = 3 \bullet (\mathbf{u}_{i+1} \bullet \mathbf{A}_1 - \mathbf{A}_2 \bullet \mathbf{u}_i - \mathbf{A}_3 \bullet \mathbf{u}_{i-1}) - \mathbf{f}_i - \mathbf{f}_{i-1} \tag{10}$$
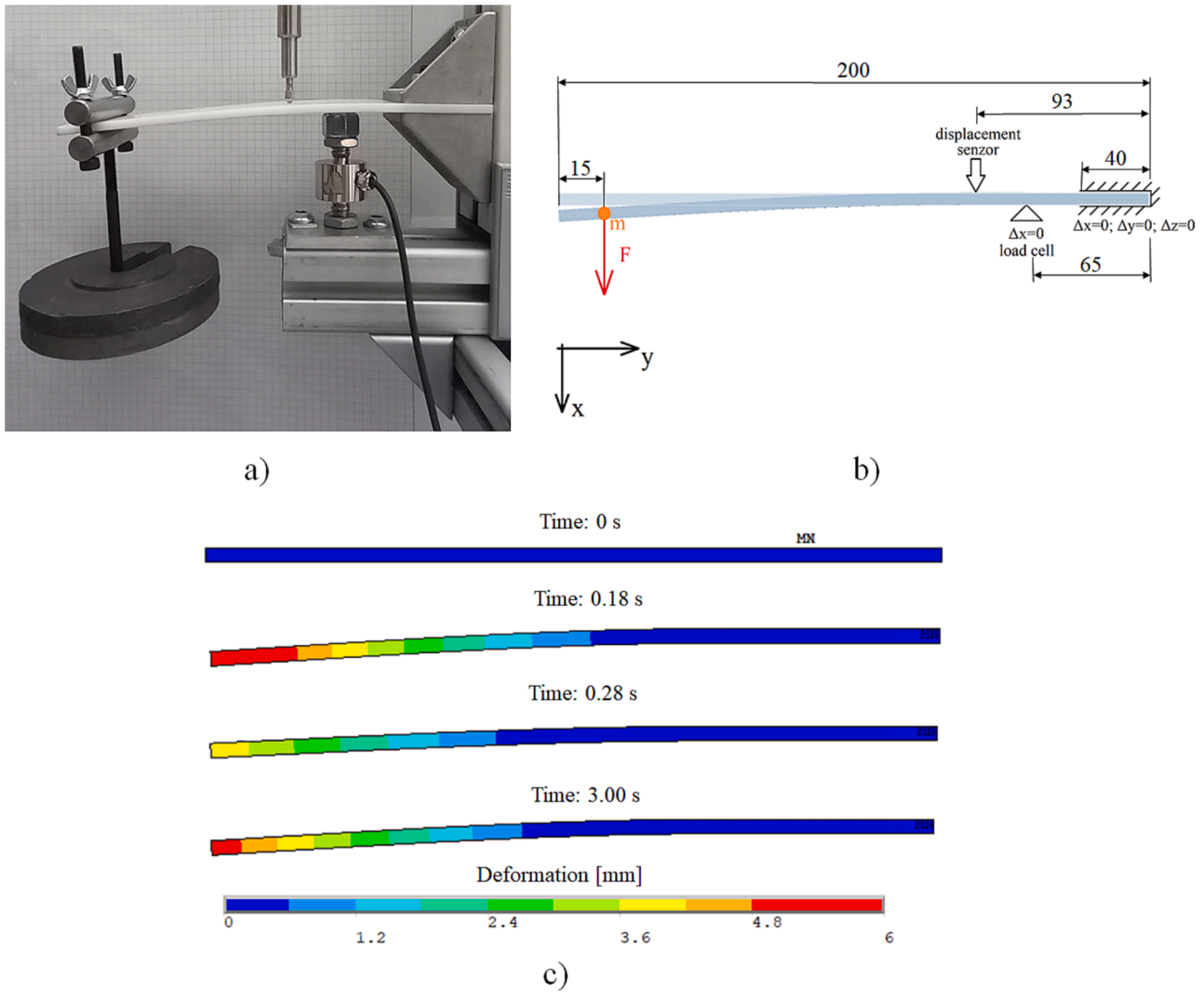
Fig. 5. FEM parameter calibration of the PMMA tool, (a) measurement, (b) simulation, (c) deformation of the PMMA tool in the FEM simulation under 1 kg load at time instants of 0 s, 1.18 s, 1.28 s, and 3.00 s (dimensions are given in mm).

The force vector acting on the nodes in time step i + 1 can provide information about the forces acting at the locations of any constraints (e.g. clamping, load cell). Therefore, the reaction forces at the location of the load cell can be directly compared to the force values, which were measured empirically.

2.6. Initialization and reduction of the FEM model

To perform the numerical calculations presented earlier, it is necessary to determine the mass matrix **M** and stiffness matrix **K** for the soil-engaging tool. This task is accomplished during the pre-processing of the FEM simulation, which is conducted using Ansys Mechanical APDL®. The input parameters of the pre-processing are the geometry of the soil-engaging tool, its material properties, the material models applied, and the boundary conditions. The FEM preprocessor first discretizes the tool under analysis, which is done by meshing the model. The resulting mass and stiffness matrices will thus be related to the displacements and loads of these mesh nodes. In the FEM meshing process, the mesh describing the tool geometry imported from the DEM simulation is supplemented by new nodes, as illustrated in Fig. 2. Employing the nomenclature used in Ansys Mechanical APDL®, the initial geometry is described by keypoints, while the FEM mesh of the tool is described by the nodes.

The EDEM Coupling Interface can only handle the loads and displacements of the keypoints (Fig. 2a) that describe the original geometry. In contrast, the mass and stiffness matrices computed by the FEM preprocessor include the new nodes generated in the meshing process. As a result, these matrices cannot be directly used in the two-way coupling. The substructuring technique provides a solution to this problem by allowing the FEM model to be reduced solely to the keypoints (Mandel, 1990; Wang and Jagfeld, 1993; Weng et al., 2011). To apply this method, let us consider the following block matrix form of the stiffness equation:

$$\begin{bmatrix} \mathbf{K}_{aa} & \mathbf{K}_{ab} \\ \mathbf{K}_{ab} & \mathbf{K}_{bb} \end{bmatrix} \begin{bmatrix} \mathbf{u}_a \\ \mathbf{u}_b \end{bmatrix} = \begin{bmatrix} \mathbf{f}_a \\ \mathbf{f}_b \end{bmatrix} \tag{11}$$

where the displacement and force values associated with the keypoints are located in the elements $\mathbf{u}_a$ and $\mathbf{f}_a$, while the displacements and forces of the remaining nodes are in $\mathbf{u}_b$ and $\mathbf{f}_b$, respectively. Accordingly, the stiffness matrix can also be divided into four submatrices, which include the cross-couplings between the keypoints and the nodes that are not keypoints. Expanding the second row of the block matrix equation yields the following equation:

$$\mathbf{K}_{ba}\mathbf{u}_a + \mathbf{K}_{bb}\mathbf{u}_b = \mathbf{f}_b \tag{12}$$

If the active loads and constraints act only on the keypoints, then the

Table 2
Micromechanical DEM parameters.

Particle/Body/ Interaction type	Property	Value	Source
Particle	d (mm)	$9.95 - 10.05$	selected
	Size distribution	random	Ucgul et al., 2015
	$\rho_{particle}$ (kg m^{-3})	2600	Huser and Kvernvold, 1998
	$E_{particle}$ (Pa)	$1.12 \bullet 10^{10}$	Ucgul et al., 2015
	$G_{particle}$ (Pa)	$4.30 \bullet 10^{10}$	Ucgul et al., 2015
	$\nu_{particle}$ (-)	0.3	Asaf et al., 2006
	Y (Pa)	$5.88 \bullet 10^{5}$	Ucgul et al., 2015
PMMA tool	$\rho_{DEMPMMA}$ (kg m^{-3})	1220	measured
	$E_{DEMPMMA}$ (Pa)	$7.90 \bullet 10^{10}$	Ucgul et al., 2015
	$G_{DEMPMMA}$ (Pa)	$2.05 \bullet 10^{11}$	Ucgul et al., 2015
	$\nu_{DEMPMMA}$ (-)	0.3	Ucgul et al., 2015
Soil bin and S235 tool	$\rho_{DEMsteel}$ (kg m^{-3})	7933	measured
	$E_{DEMsteel}$ (Pa)	$7.90 \bullet 10^{10}$	Ucgul et al., 2015
	$G_{DEMsteel}$ (Pa)	$2.05 \bullet 10^{11}$	Ucgul et al., 2015
	$\nu_{DEMsteel}$ (-)	0.3	Budynas and Nisbett, 2011
Particle-particle contact	e_{pp} (-)	0.6	Wang et al., 2008
	γ_t (-)	0.85	calibrated
	b_n (-)	0.5	calibrated
	k (J m^{-3})	$3.00 \bullet 10^{4}$	calibrated
Particle-soil bin, particle-S235 tool, particle-PMMA tool and particle-penetrometer contact	e_{sp} (-)	0.6	Ucgul et al., 2015
	μ_{sp} (-)	0.1	calibrated
	μ_{0sp} (-)	0.3	calibrated
General	Δt_{DEM} (s)	$7.93 \bullet 10^{-7}$	calibrated

condition $\mathbf{f}_b = 0$ holds, which allows the calculation of the displacements of nodes which are not keypoints using the following equation:

$$\mathbf{u}_b = -\mathbf{K}_{bb}^{-1}\mathbf{K}_{ba}\mathbf{u}_a \qquad (13)$$

Expanding the first row of the block matrix equation, the following equation is obtained:

$$\mathbf{K}_{aa}\mathbf{u}_a + \mathbf{K}_{ab}\mathbf{u}_b = \mathbf{f}_a \qquad (14)$$

Substituting Eq. (13) and extracting $\mathbf{u}_a$ from Eq. (14) the following equation is obtained:

$$\underbrace{\left(\mathbf{K}_{aa} - \mathbf{K}_{ab}\mathbf{K}_{bb}^{-1}\mathbf{K}_{ba}\right)}_{\mathbf{K}}\underbrace{\mathbf{u}_a}_{\mathbf{u}} = \underbrace{\mathbf{f}_a}_{\mathbf{f}} \qquad (15)$$

which only contains the displacement and force vector of the keypoints.

By utilizing the substructuring method in this way, the dynamic finite element equation describing the relationship between the displacement vector and the force vector of the keypoints can be derived. It is important to note that this method can be validly applied only if there are no external loads or constraints acting on nodes that are not keypoints. Therefore, during preprocessing in Ansys®, only the degrees of freedom of keypoints should be constrained. Similar calculations can be performed for the mass matrix, and the results obtained in this way can be used with the EDEM coupling interface for the two-way DEM-FEM coupling.

2.7. DEM-FEM simulation cycle

The sequential diagram of the coupled DEM-FEM simulation procedure is shown in Fig. 3, illustrating the types of software that were applied and the interactions between them. Since nowadays an increasing number of soil studies are being carried out using Altair EDEM® (Ucgul et al., 2017; Zhang et al., 2023), the DEM calculations were performed using this software. The pre-processing of the FEM model was accomplished by Ansys Mechanical APDL®, and the coupling

and FEM calculations were carried out by an in-house developed coupling client built on the EDEM coupling interface.

The simulation process consists of the following steps: (1) The coupling client retrieves the deformable tool geometry used in the DEM simulation via the coupling API. (2) The coupling client generates an APDL script that is read and executed by Ansys®. This script creates the tool geometry in Ansys®. (3) The user specifies the element type, material properties and boundary conditions, then performs meshing on the Ansys® user interface. (4) The coupling client generates additional APDL scripts that are read and executed by Ansys®. These scripts perform FEM preprocessing and substructuring analysis, exporting the results to a file. (5) Next, the coupling client reads the file generated by Ansys®, which contains the necessary stiffness and mass matrices. (6) The coupling client then retrieves the nodal forces acting on the tool. (7) Finally, the coupling client calculates the deformations based on the FEM equations and matrices and sends them back to EDEM®. The simulation cycle then repeats from step 6. This sequence of steps is repeated iteratively during the coupled DEM-FEM simulation.

2.8. Simulation cases

The measurements were simulated using DEM and two-way coupled DEM-FEM. To model the sandy soil, the hysteretic-spring DEM contact model was applied, supplemented with the linear cohesion secondary model, similar to Ucgul et al. (2015) and Bahrami et al. (2020). Artificial damping (Wang and Yan, 2012) was not included in the model, only viscous damping from particle-particle and particle-geometry contacts was considered, similarly to the work of Horváth et al. (2022). A linear elastic FEM material model was selected for modelling the deformation of the soil-engaging tools. The simulations were performed on an Intel® Core™ i7-9700 3 GHz processor with 32 GB RAM, using Altair EDEM 2020® software and a FEM coupling client that was developed in-house. Three variants were investigated: Firstly, the measurements related to the S235 tool were modelled using a DEM simulation, treating the tool as a rigid body. Secondly, the measurements of the S235 tool were
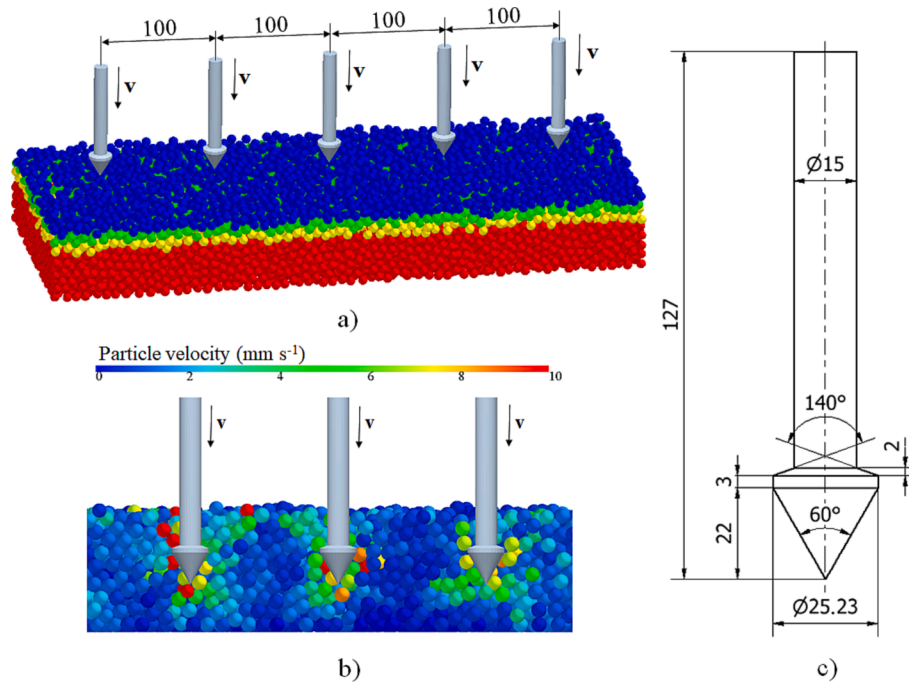
Fig. 6. Penetrometer simulation (a) initial position, (b) velocity field of the particle assembly around three neighbouring penetrometers at a depth of 55 mm. (c) Penetrometer geometry with a projected cross-sectional area of 5 cm^2 (v = 10 mm s^{-1} indicates the direction of penetrometer velocities, dimensions are in mm).
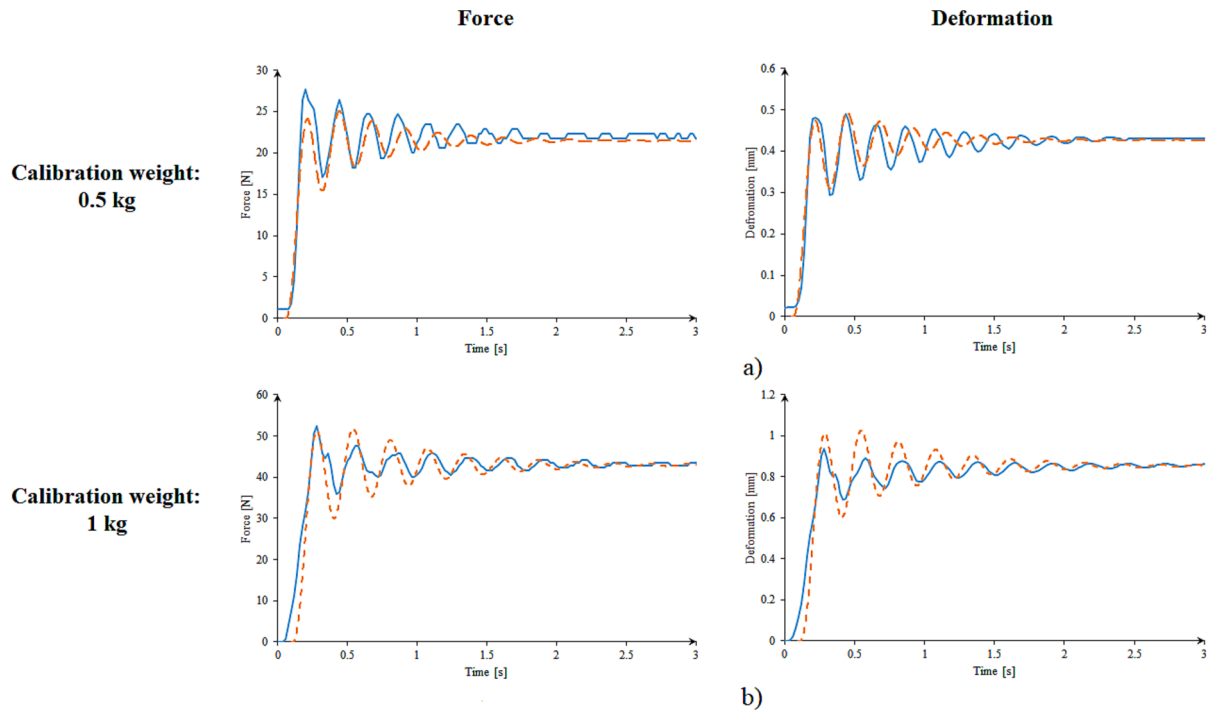
Fig. 7. FEM calibration of the PMMA tool, (a) force acting on the tool, (b) deformation of the tool, – measurement, - - simulation.

modelled using a coupled DEM-FEM simulation, taking into account the deformation of the tool. Thirdly, the measurements with the PMMA tool were modelled using a coupled DEM-FEM simulation, also taking into account the deformation of the tool.

In all the cases, the simulations were run at three working depths, which corresponded with the measurements used (18 mm, 30 mm and 42 mm). The required computational times of the DEM simulations and

the coupled DEM-FEM simulations for different tools and at different working depths are presented in Table 1.

2.9. Simulation model of the soil-passively vibrating tool interaction

At the beginning of the simulations, a discrete element assembly was created using gravitational deposition, as shown in Fig. 4b, with
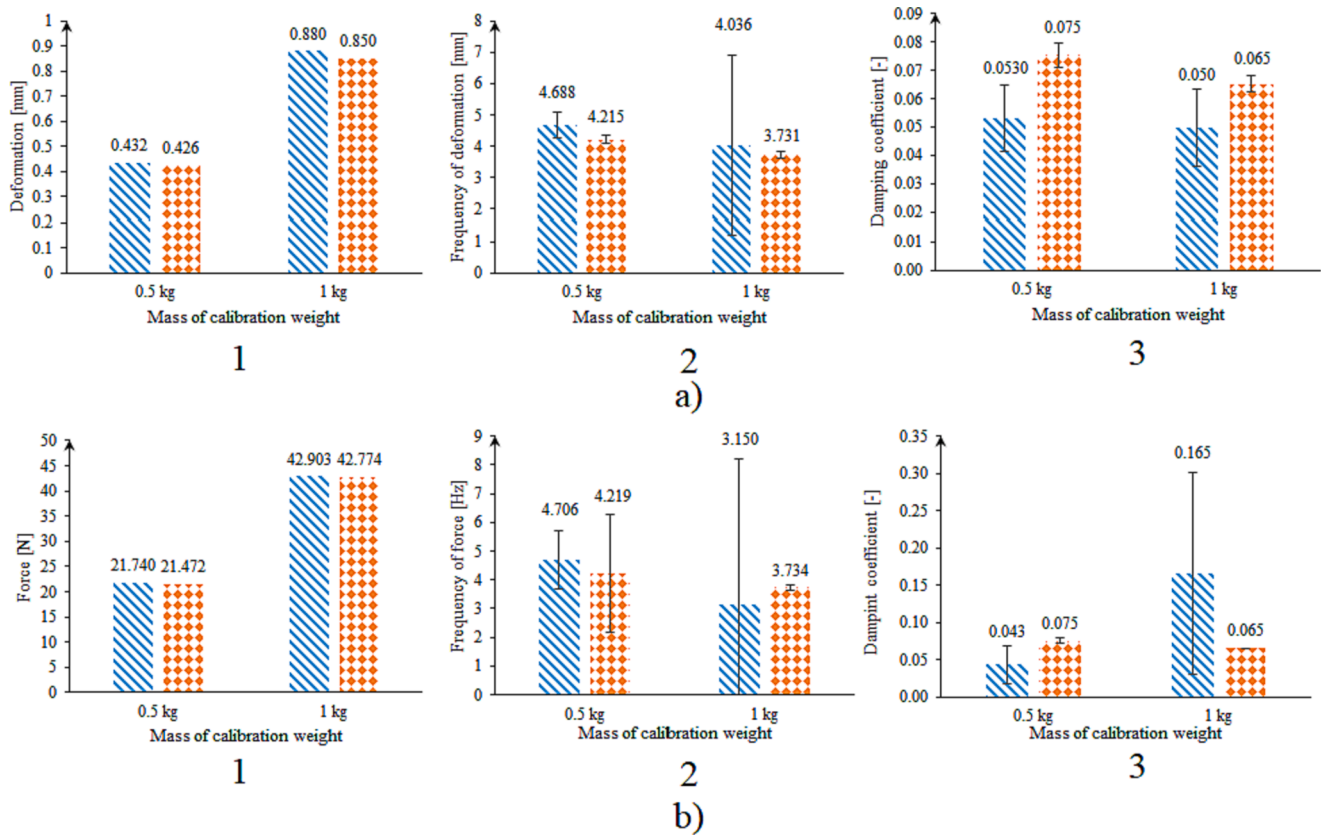
Fig. 8. Numerical comparison of the FEM parameter calibration ▨ measurement and ❖ simulation of PMMA tool, a) deformation data, b) force data, 1: steady-state value, 2: mean frequency, 3: damping factor (vertical segments indicate the standard deviation of frequency and damping data).

Table 3
Macromechanical FEM parameters.

Body	Property		Source
PMMA tool	α_{PMMA} (-)	0.55	calibrated
	β_{PMMA} (-)	0	selected
	$E_{FEMPMMA}$ (Pa)	$4.06 \bullet 10^9$	calibrated
	$\nu_{FEMPMMA}$ (-)	0.38	Ridwan-Pramana et al., 2017
	$\rho_{FEMPMMA}$ (-)	1220	measured
S235 tool	α_{steel} (-)	0.55	calibrated
	β_{steel} (-)	0	selected
	$E_{FEMsteel}$ (Pa)	$2.07 \bullet 10^{11}$	calibrated
	$\nu_{FEMsteel}$ (-)	0.3	Dratt and Katterfeld, 2017
	$\rho_{FEMsteel}$ (kg m^{-3})	7933	measured
General	Δt_{FEM} (s)	0.001	calibrated

spherical particles ranging from 9.5 to 10.5 mm in diameter and a random particle size distribution. To reduce the computational time, a smaller assembly size was used in the simulations compared to the real measurements, similar to in the research by Zeng et al. (2017). The assembly had the same width (250 mm) and length (650 mm) as the soil bin, but unlike the bin used for measurements of sandy soil, which was 112 mm high, the discrete element assembly was created with a height of only 85 mm. This did not affect the results of the simulation because even at the maximum working depth, the soil-engaging tool did not have any influence on the motion of the lower particles, as shown in Fig. 4c and d. At the upper 30 mm level, layers were deposited at 10 mm intervals, creating a total number of four layers for the entire assembly, each indicated by a different colour (Fig. 4a). Following the creation of the layered DEM assembly, the geometries of the soil-engaging tools were separately imported into the simulation domain as surface models, their surfaces were meshed using 5 mm triangular elements (Fig. 4e), and were inserted into the discrete element assembly in a vertical

direction.

In the FEM model of the soil-engaging tools (Fig. 5b), all degrees of freedom were restrained within the clamped section, i.e. the top 40 mm of the tools. At the contact point of the load cell, located below the top of the tools in the same position as in the measurements, the displacements in the direction of the tool velocity (z direction) were fixed. In the DEM-FEM simulations the reaction forces present at this constraint were calculated, thus allowing the simulated force values to be directly compared with the force values measured with the load cell. However, as there was no FEM calculation in the DEM simulation of the S235 tool, the forces acting on the load cell could not be directly calculated. Instead, the forces acting on the load cell were calculated from the particle-tool interaction forces of the DEM simulation, taking into account the equilibrium of the rotational momentum, i.e. the lever effect, at the clamped section of the tool. In the simulation, unlike in reality, the soil bin was not moved, but instead the linear motion was imposed on the soil-engaging tools. However, this did not affect the comparability of the simulation and reality, as the same relative velocity was considered between the tools and the soil bin in both the measurements and simulations. Furthermore, the low velocities (maximum of 36.14 mm s^{-1}) ensured that the acceleration and deceleration present at the beginning and end of the measurement did not appreciably affect the comparability of the measurement and simulation.

2.10. Calibration procedure

2.10.1. FEM parameter calibration

The FEM parameters of the soil-engaging tools were determined by calibration measurements using various different weights (Fig. 5a). During the calibration measurements, one end of the tool was clamped at the same position as in the soil bin measurements, in a horizontal position, and supported by a load cell underneath. An apparatus with a
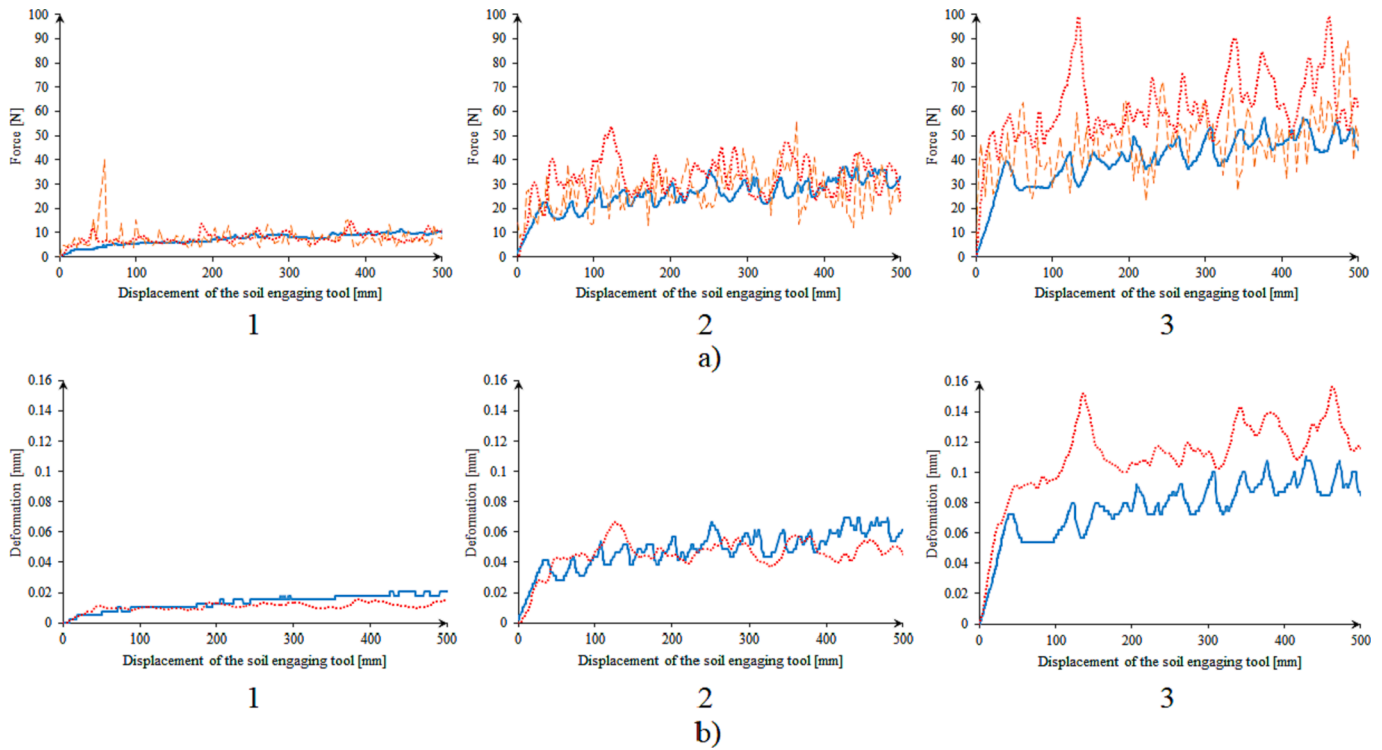
Fig. 9. Results of the – (RGB 91, 155, 213) measurements, - - (RGB 237, 125, 49) DEM simulations and ⋯ (RGB 255, 0, 0) DEM-FEM simulations of the S235 tool, a) forces, b) deformations, in 1: 18 mm, 2: 30 mm, 3: 42 mm working depth.

Table 4
Calibrated static and rolling friction coefficients of the different layers.

		layer1 (to 10 mm depth)	layer2 (in 10–20 mm depth)	layer3 (in 20–30 mm depth)	layer4 (in 30–85 mm depth)
layer1 (to 10 mm depth)	static friction (-)	0.07	0.07	0.07	0.07
	rolling friction (-)	0.02	0.02	0.02	0.02
layer2 (in 10–20 mm depth)	static friction (-)	0.07	0.07	0.07	0.07
	rolling friction (-)	0.02	0.02	0.02	0.02
layer3 (in 20–30 mm depth)	static friction (-)	0.07	0.07	0.21	0.21
	rolling friction (-)	0.02	0.02	0.07	0.07
layer4 (in 30–85 mm depth)	static friction (-)	0.07	0.07	0.21	0.3
	rolling friction (-)	0.02	0.02	0.07	0.2

pan was attached to the other end of the tool, onto which the calibration weights were hung. While the measurements were being taken, the deformation of the tool was measured using a displacement sensor and the force acting on the tool was measured using a load cell located at the same position as in the soil bin measurements.

The dynamic parameters of the PMMA tool were determined by instantaneously hanging calibration weights on the pan and simultaneously measuring the force acting on the tool and the deformation of the tool. The measurements were conducted with two different loads: 0.5 kg and 1 kg. The process was simulated using our in-house developed FEM coupling client software (Fig. 5b). In the Rayleigh damping matrix, the component (β_{PMMA}), which is proportional to the mass matrix, was set at 0 in the interest of simplification, and the Poisson's ratio was adopted from the literature (Ridwan-Pramana et al., 2017). The density of the tool was measured using a digital scale, with 1 g accuracy, and the Young's modulus, as well as the component (α_{PMMA}) proportional to the stiffness matrix in the damping matrix was adjusted until a close agreement with the measurements was achieved. In the simulation, the calibration weights were considered to be uniformly distributed loads in the rows of the force vector where the apparatus with the pan supporting the weights was in contact with the tool. Additionally, the mass of the calibration weights was considered by mean of a lumped mass matrix

which was added to the main diagonal of the tool's mass matrix in the same rows where the loads were applied in the force vector (Fig. 5b). It should be noted that using a lumped mass matrix instead of a consistent mass matrix is a simplification (Wu, 2006), although in this research the deviations caused by this simplification were deemed acceptable. Displacement boundary conditions were applied by fixing all degrees of freedom of the FEM nodes at the clamping location and fixing the displacement in the direction of the tool velocity at the position of the load cell.

For the S235 tool, the density was measured using a digital scale, but only the parameter associated with the static state, which is the Young's modulus, was determined through calibration measurements. It was not possible to measure the vibration frequency and Rayleigh damping components of the S235 tool, because its vibration frequency exceeded the measurement limits of our instruments. For this reason, instead of measurement, the Poisson's ratio was adopted from the literature and the Rayleigh damping coefficients were set at the same values as those applied in the case of the PMMA tool. It should be noted that this was a simplification, which in this case did not lead to any major deviations between the measured and simulated data, although in the future the more precise determination of these parameters could be a subject for further study. The measurement setup and simulation procedure were
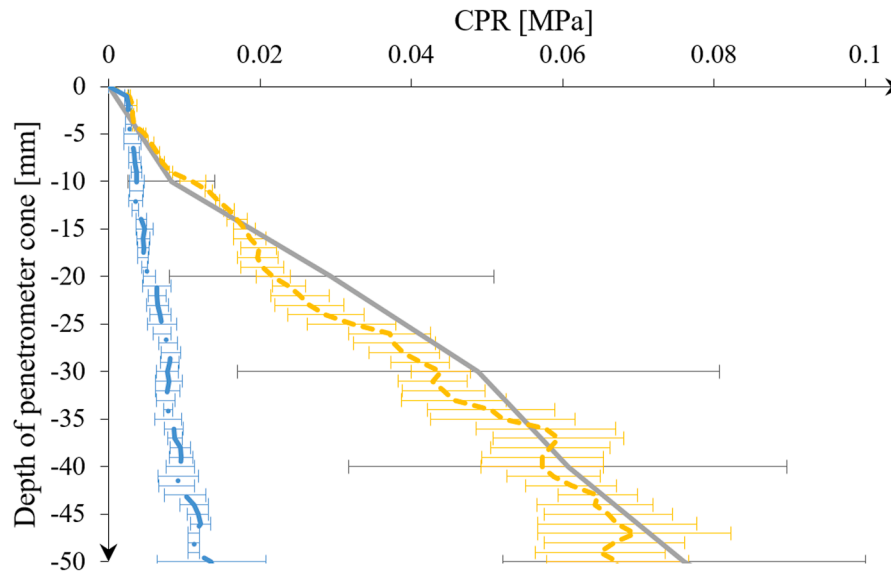
Fig. 10. Mean values and standard deviations of the cone penetration resistance (CPR) – (RGB 165, 165, 165) tests, -- (RGB 165, 165, 165) simulation with layered particle assembly, -·- (RGB 91, 155, 213) simulation with non-layered particle assembly.

similar to those used for the PMMA tool.

2.10.2. DEM parameter calibration

Due to the high stiffness of the S235 tool, the deformation that occurred had only a negligible effect on the movement of the sandy soil. Therefore, in this case, it was possible to examine the DEM parameters separately from the FEM parameters. To determine the DEM parameters (as shown in Table 2), the soil bin measurements performed with the S235 tool were utilized.

The parameter calibration started by assigning the same material parameters to all the particles, and the parameters were adjusted until good agreement was achieved with the measurements made for the S235 tool at a depth of 18 mm. The proper agreement was achieved by adjusting the static and rolling friction coefficients. After obtaining the parameter combination, the simulation was run at a depth of 30 mm, but it was observed that the simulation underestimated the measured force by an average of 30 %. This led us to conclude that creating a DEM assembly with a single parameter combination is not sufficient. As such, to achieve good agreement with the measurements at all three depths, a multi-layer soil model would be required (Tamás and Bernon, 2021). Therefore, the DEM assembly was divided into four layers, and different material parameters were assigned to each layer.

The calibration was performed by adjusting the static and rolling friction parameters, using the results from the empirical measurements at all three depths. When progressing from the uppermost depth to the lowest depth, the friction parameters of the lowest layer in contact with the tool were determined at each depth. Since in the simulation of a previous, shallower depth, the tool had not come into contact with the lowest layer at the next depth, adjusting the friction coefficients of this layer did not affect the simulation results at shallower depths. When employing this method, good agreement was achieved with the measurements in the DEM simulations at all three depths. It should be noted that it is likely that various possible parameter combinations could have resulted in a good agreement with the measurements (Roessler et al., 2019). However, it was not the aim of the present study to find all the possible parameter combinations that could produce agreement with the measured data.

We also conducted coupled DEM-FEM simulations of the S235 tool using the calibrated DEM and FEM parameters, taking into account the deformation of the tool. This allowed us to examine the influence of tool deformation on the motion of the DEM particles.

The DEM parameters that were taken from the literature, measured, selected or calibrated are shown in Table 2. The time step was calculated using the Rayleigh time-stepping method, which can be regarded as a rough estimate (Tamás, 2018). The simulations were stable and yielded satisfactory results when using 20 % of the Rayleigh time step ($7.93 \bullet 10^{-7}$ s). Therefore, the DEM simulations and the DEM part of the coupled DEM-FEM simulations were performed using this time step.

2.10.3. Validation of the calibrated DEM parameters

In addition, to validate the calibrated parameter combination, the penetration resistance of the sandy soil was measured at 5 randomly selected locations within the soil bin. For this purpose, a cone penetrometer instrument (06.15.SA, Royal Eijkelkamp B.V., Netherlands) with a projected cross-sectional area of 5 cm^2 and a cone angle of 60° (Fig. 6c) was used (Tamás and Bernon, 2021). The measurements were conducted at a speed of lower than 20 mm s^{-1}, following the ASABE standards (ASABE Standards, 2006a; ASABE Standards, 2006b). The measurements were also simulated using DEM, with the same geometry and measurement parameters as in the empirical measurements. In order to prove the necessity of defining layers in the DEM particle assembly, two cone penetrometer simulations were carried out. In the first simulation, the whole particle assembly had the friction parameters of layer1 (Fig. 4a), which had been obtained from the previous calibration procedure (non-layered particle assembly). In the second simulation 4 layers were defined as shown in Fig. 4a and Fig. 6a, and the layers had the friction parameters obtained from the previous calibration procedure (layered particle assembly). In both simulations, in addition to the friction parameters, all other parameters were obtained from the previous calibration procedure (Table 2). In the simulations, 5 penetrometer geometries (Fig. 6a) were placed at intervals of 100 mm and simultaneously moved downward, and the average and deviation values of the vertical forces acting on the penetrometer geometries were calculated. This allowed the uncertainty in the simulation results to also be taken into account. Furthermore, to quantitatively compare the deviations of the measurements and simulations, the standard deviation values were divided by the mean values at each data point, and the values thus obtained were averaged along the measured and simulated mean curves. These average values, which can be expressed as a percentage, were designated as "mean deviation". The information obtained from the penetrometer measurements and from the simulations provided insights into the heterogeneity of the soil and into the cone
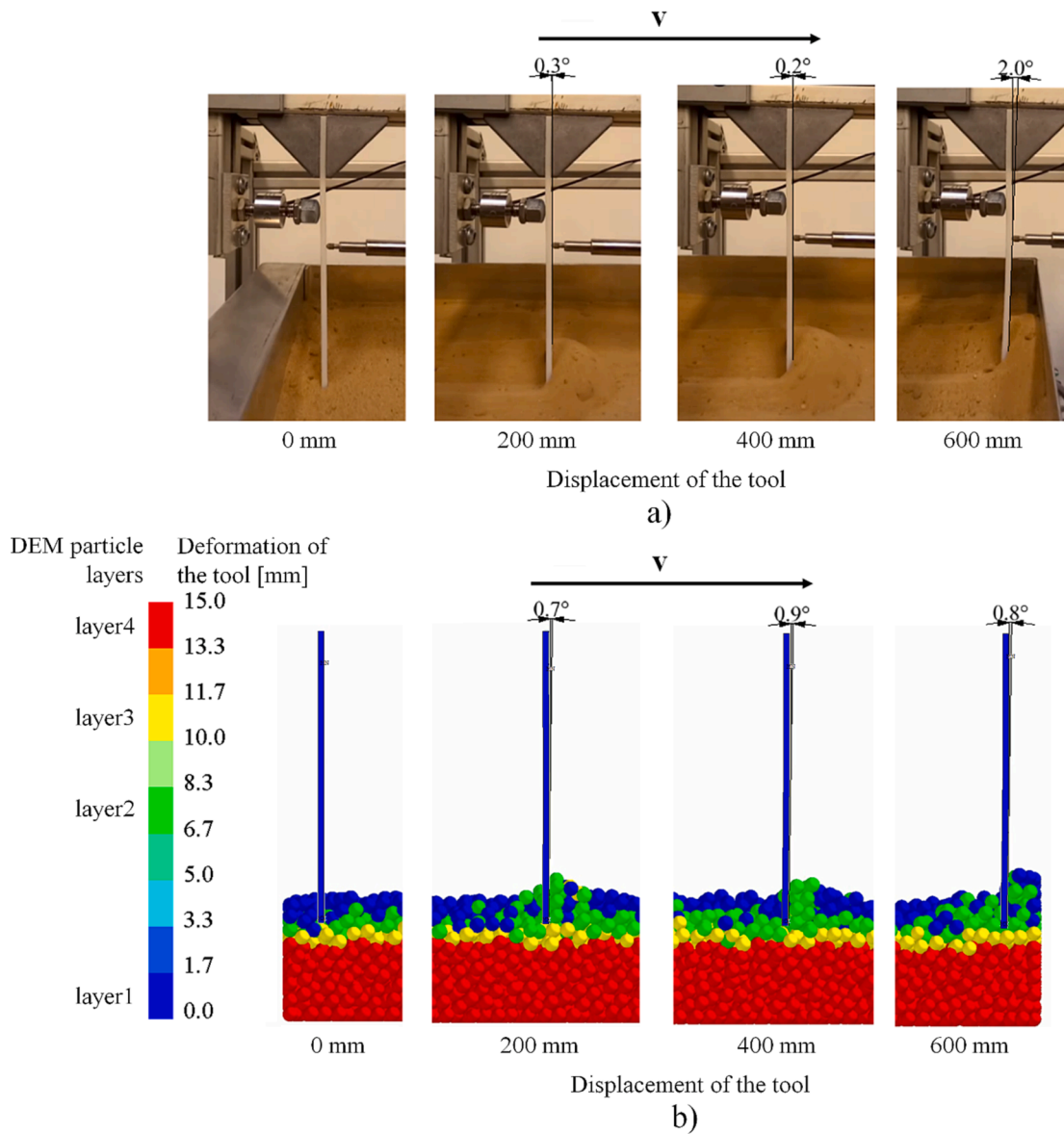
Fig. 11. Deformation of the PMMA tool at a working depth of 18 mm during a) measurement and b) simulation (the relative velocity of the tool with respect to the soil bin is indicated by vector $\mathbf{v} = 36.1$ mm s^{-1}, moreover the DEM particle layers and the deformation of the tool is colour scaled).

penetration resistance (CPR), which was calculated as the ratio of the force acting on the penetrometer to the projected cross-sectional area of the cone (Tamás and Bernon, 2021). Fig. 6b) shows the velocity field of the particle assembly at a depth of 55 mm in the vicinity of three neighbouring penetrometers in the simulation.

3. Results

3.1. FEM calibration results

Fig. 7 shows the fluctuations in both the empirically measured and the simulated force and deformation values for the PMMA tool over time for the two calibration weights. To facilitate comparison between them, the simulation curves were shifted on the time axis so that the first local maximum values coincide in time (Suhr and Six, 2017; Szabó et al., 2022).

It can be observed that the measured and simulated results closely match. To numerically compare the results, a correlation coefficient (Asuero et al., 2006) was calculated between the measured and simulated curves using the built-in correlation function of Microsoft Excel

2013®. The measured and simulated force curves had correlation values of 0.93 and 0.95 in the case of the 0.5 kg weight and the 1 kg calibration weight, respectively. The measured and simulated deformation curves had correlation values of 0.94 and 0.95 in the case of the 0.5 kg and 1 kg calibration weight, respectively. Furthermore, to compare the static and vibration parameters of the simulation and the measurement, the steady-state values, the frequencies, as well as the damping values for both the measured and simulated data were calculated (Fig. 8). The vibration frequencies and damping values were calculated based on data from multiple cycles, and their standard deviations are also shown in the diagram (Fig. 8a.1, a.3, b.2 and b.3).

In the steady-state condition, the simulated results show good agreement with the measurements (Fig. 8a.1 and b.1). The maximum deviation is observed in the deformation of 3.4 %, when the 1 kg calibration weight was applied (Fig. 8a). The measured and simulated frequencies are also in good agreement (Fig. 8b and e). The largest deviation in the frequency of the force between the measured and simulated values (18.6 %) was observed with the 1 kg calibration weight (Fig. 8b). This deviation can be attributed to the high number of deviations in the measured data. The agreement between the measured
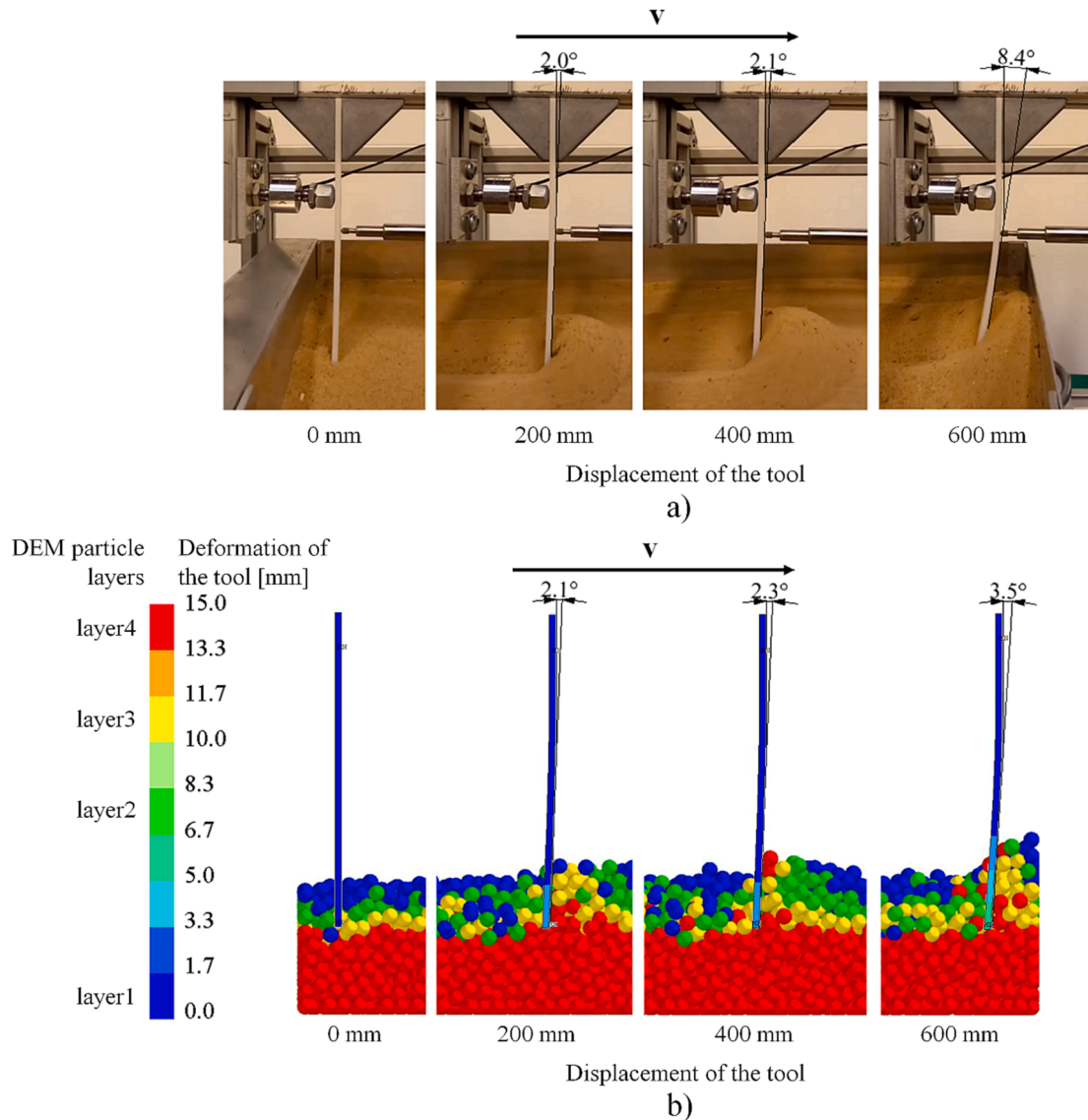
Fig. 12. Deformation of the PMMA tool at a working depth of 30 mm during a) measurement and b) simulation (the relative velocity of the tool with respect to the soil bin is indicated by vector **v** = 36.1 mm s^{-1}; moreover the DEM particle layers and the deformation of the tool is colour scaled).

and simulated results is less satisfactory for the damping values (Fig. 8c and f). This could be improved with further iterations or by utilizing an artificial intelligence-assisted calibration approach, such as by using genetic algorithms, to achieve a more accurate match. Based on the results of the calibration process, the determined parameter values (Table 3) were deemed to be acceptable.

3.2. DEM calibration results

The measurements, DEM simulation, and the coupled DEM-FEM simulations of the S235 tool at the three investigated working depths are shown in Fig. 9 and in the videos available online as additional material. By appropriately selecting the static and rolling friction coefficients within and between layers (Table 4), at the end of the parameter calibration, the average results of the simulations and measurement data were brought into good agreement at all three working depths. However, in the simulations, the forces acting on the tool exhibited greater fluctuations. This can be attributed to the fact that in the simulation the soil was modelled with particles that were much larger than the sand grains, which interacted with the tool discretely at specific time points rather than continuously (Tamás, 2018).

Furthermore, for the 42 mm working depth, it can be observed that the coupled DEM-FEM simulations overestimated the force acting on the tool and the deformation of the tool, indicating that the coupled DEM-FEM simulations can provide accurate estimations of the tool's behaviour only within a certain range of working depths. Since contact is possible between any two different layers or between particles within the same layer, it was necessary to define the static and rolling friction coefficient pairs for all layers and between all layers (Table 4).

3.3. Cone penetration results

To verify the calibrated DEM parameters and to show the necessity of including layers in the DEM simulation, the mean values and standard deviation values of the measured and simulated Cone Penetration Resistance (CPR) data were compared (Fig. 10). It can be observed that while the simulated CPR values of the non-layered particle assembly were underestimated in comparison with the measured CPR values, the simulated CPR values of the layered particle assembly exhibit good agreement with the measured CPR values, as the simulation data falls within the range of deviation of the measurement data at every depth. Therefore, it can be concluded that the discrete element parameters of
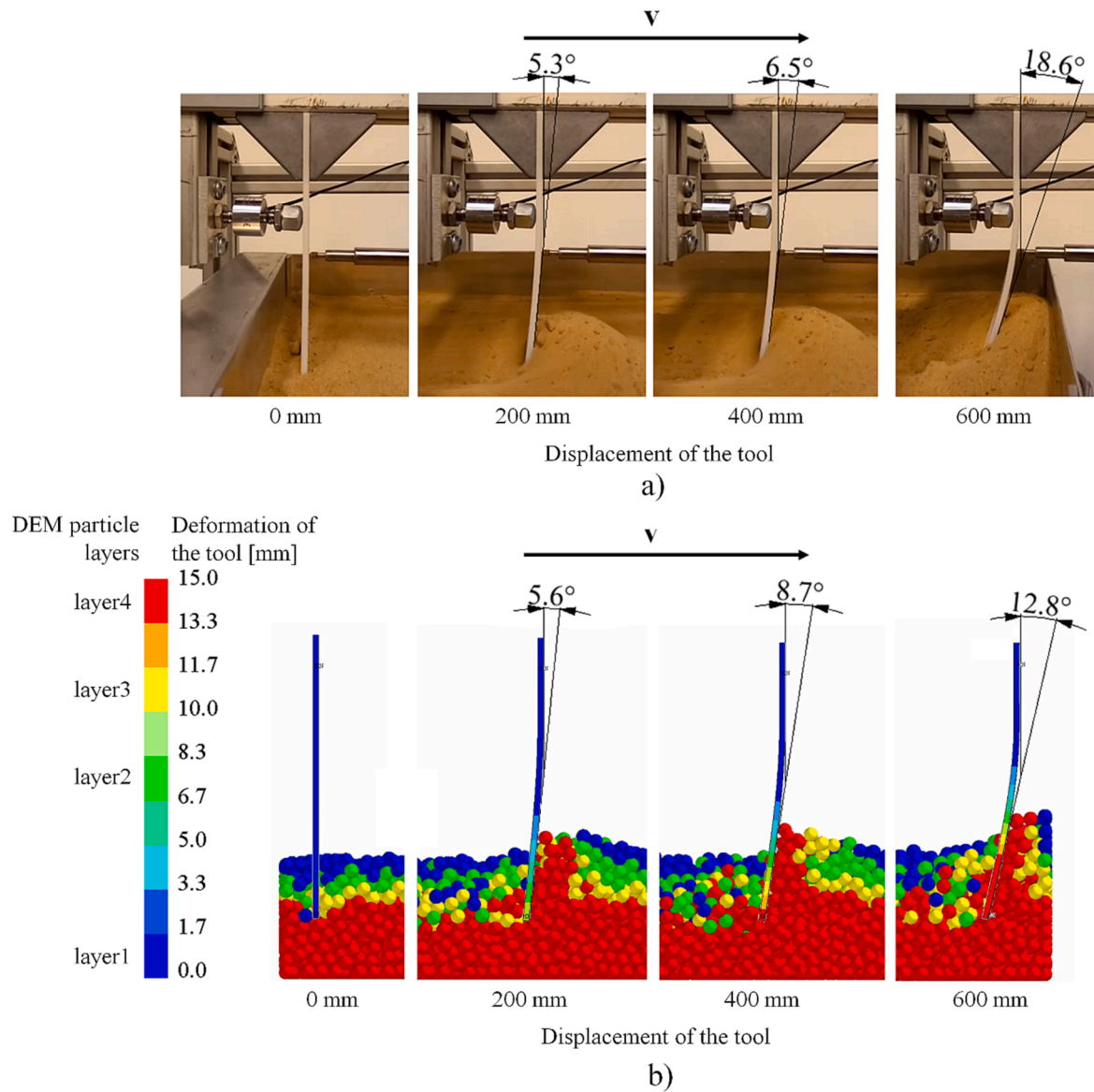
Fig. 13. Deformation of the PMMA tool at a working depth of 42 mm during a) measurement and b) simulation (the relative velocity of the tool with respect to the soil bin is indicated by vector **v** = 36.1 mm s^{-1}, moreover the DEM particle layers and the deformation of the tool is colour scaled).
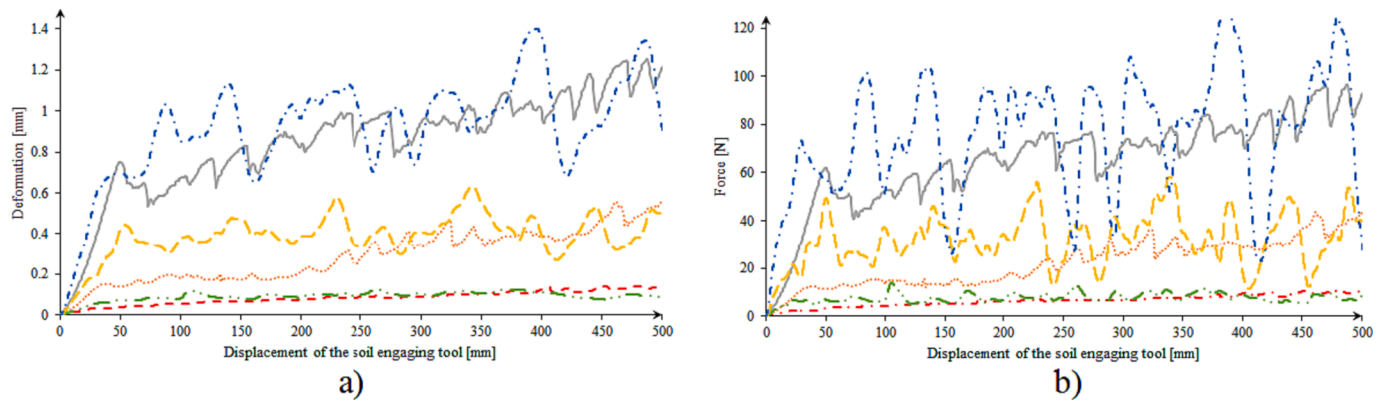

Fig. 14. Deformations and forces acting on the PMMA tool a) deformations in the function of tool displacement, b) forces acting on the PMMA tool in the function of tool displacement, -- (RGB 255, 0, 0) measurement in 18 mm working depth, ··· (RGB 237, 125, 49) measurement in 30 mm working depth, — (RGB 165,165,165) measurement in 42 mm working depth, -··- (RGB 112, 173, 71) simulation in 18 mm working depth, - - (RGB 255, 192, 0) simulation in 30 mm working depth, -·- (RGB 68, 114, 196) simulation in 42 mm working depth.
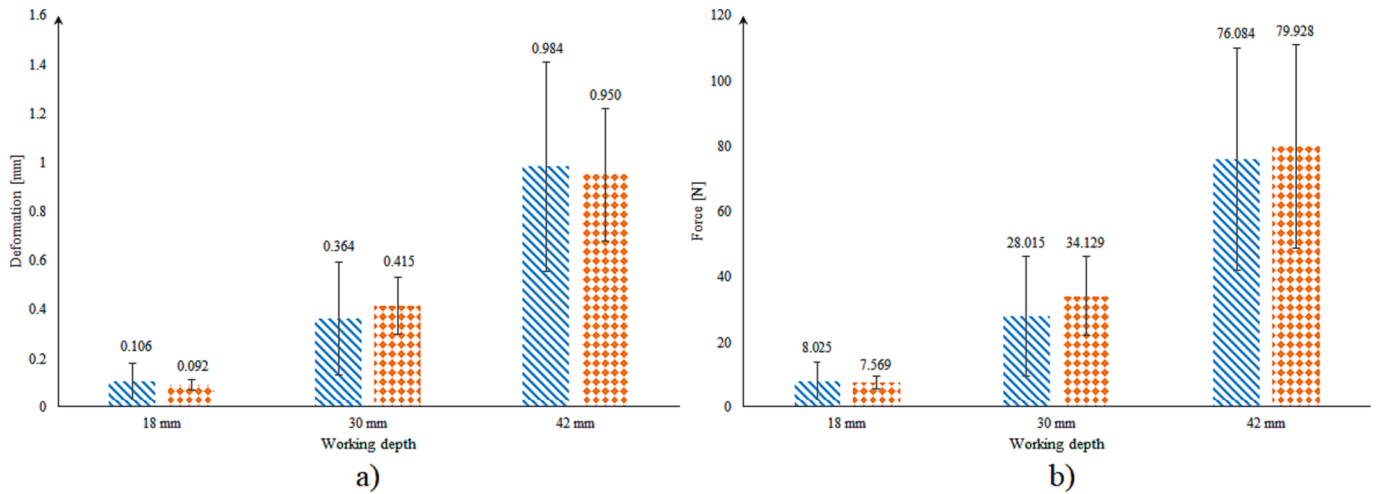
Fig. 15. Numerical comparison of ▨ measured and ⁜ simulated a) mean deformation, b) mean force values in the three examined working depths, in the range of 100–500 mm tool displacement (vertical segments indicate the standard deviation of the data).

the sandy soil were adequately determined by the calibration of the S235 tool, which utilised four different particle layers in the DEM assembly. The standard deviation values indicate the variations between different measurements and different simulations. The mean deviation of the measurement data is ±30 %, while the mean deviation of the simulation data is ±10 %. To achieve a more precise match in deviation values, adjustments to the particle size distribution might be required, but this would increase the computational demands of the simulation. However, even when considering the current results, it can be seen that the heterogeneity of the soil, as shown by the different results obtained at different locations of the soil bin, can be modelled in the DEM simulation, which is an advantage in the application of this method. The simulation was run only up to a displacement of 55 mm, primarily because a shallower layer (85 mm) was investigated in the simulation in order to reduce computational time. Additionally, at depths greater than 55 mm, the influence of the soil bin walls became significant, resulting in a rapid increase in the amount of force acting on the penetrometer in the simulation.

3.4. DEM-FEM coupled simulation results of the PMMA tool

The results of both the simulations and the empirical measurements showed the PMMA tool deform in a similar way, which can be seen in Figs. 11–13, and in the videos available online as additional material. However, the simulated deformation values did not consistently match the measurement at every time step. This can be attributed to the fact that the vibrating motion of the PMMA tool was not in the same phase during the measurement and simulation. Between 200 and 400 mm of tool displacement, at an 18 mm working depth (Fig. 11), the backward tilt of the tool was measured as 0.2–0.3°, while the simulation predicted a tilt of 0.7–0.9°. At a 30 mm working depth (Fig. 12), the empirical measurements showed a tilt of 2–2.1°, while the simulation yielded 2.1–2.3°. At a 42 mm working depth (Fig. 13), the measurement resulted in a tilt of 5.3–6.5°, whereas the simulation showed a 5.6–8.7° tilt. It can be observed that in the middle of the measurement range, the simulation results are in good agreement with the measurement results. However, at 600 mm of tool displacement, the soil piled up in front of the tool to a greater extent in the measurement than it did in the simulation, leading to larger deformation in the measurement. To achieve a better agreement, further calibration of the friction coefficient pair of the particle-soil bin interaction would be required.

In the simulation, the movement of different soil layers can be observed (Figs. 11–13). It can be seen that the lowest layer that was in contact with the bottom of the tool (layer 2 at an 18 mm depth, layer 3 at

a 30 mm depth and layer 4 at a 42 mm depth) piled up in front of the tool, causing the particles to move the most compared to their initial positions. This layer had the greatest influence on the simulation. For the simulation at a working depth of 18 mm, this layer was layer 2 (green coloured) (Fig. 11), while for the simulation at a 30 mm working depth, it was a combination of layer 3 (yellow coloured) and layer 4 (red coloured) (Fig. 12), and for the simulation at a working depth of 42 mm, it was layer 4 (red coloured) (Fig. 13).

Fig. 14 shows the measured and simulated tool displacement-deformation curves, as well as the measured and simulated tool displacement-force curves of the PMMA tool. In the range of 100–500 mm of tool displacement, the simulated force data deviates from the measured data by an average of 42 %, while the simulated deformation data deviates by an average of 31 % from the measured deformation data. Furthermore, it can be observed that the deviations of force and the deformation values increase at higher mean force and deformation values. This deviation is more significant in the simulations than it was in the measurements. However, we believe that with more precise parameter calibration (e.g., by using artificial intelligence), it would be possible to also achieve similar levels of deviations in the simulations.

The mean and standard deviation of the measured and simulated deformation and force data was also calculated in the range of 100–500 mm of tool displacement (Fig. 15). It can be observed that at a working depth of 18 mm, the percentage difference between the measured and simulated mean values is always below 13 %, while at a 30 mm depth it is below 22 %, and at a 42 mm depth it is below 6 %. The mean values of the measured deformations exhibited better agreement with the simulated deformations (with a maximum difference of 14.2 %) than the mean values of the measured forces did with the simulated forces (with a maximum difference of 21.8 %). This can be attributed to the higher deviations in the simulated force values, which can be explained by the Rayleigh damping incorporated into the FEM calculations, as Rayleigh damping reduces the changes in deformation in response to the force applied to the soil-engaging tool, resulting in smaller oscillations and lower deviations in deformation compared to the force.

3.5. Comparison of the simulations

Fig. 16 shows the particle velocities with 300 mm of tool displacement for the simulations of the PMMA and S235 tool at a working depth of 42 mm. It can be observed that in the DEM-FEM simulation of the PMMA tool, the particle velocities directly in front of the tool range from 40 to 100 mm s^{-1} (Fig. 16a), in the case of the S235 tool, with the DEM-FEM simulation showing velocities of 23–40 mm s^{-1} (Fig. 16b) directly
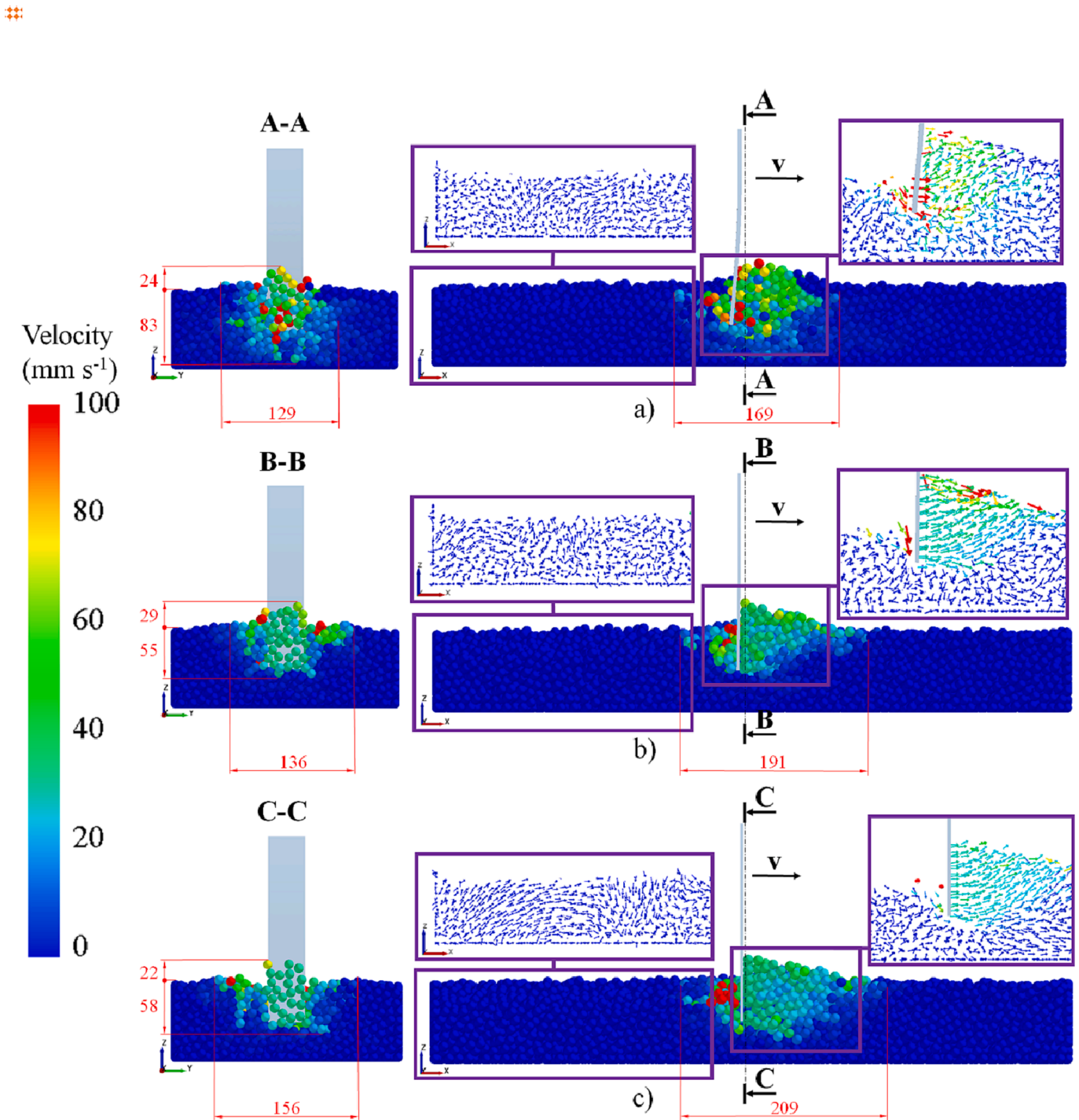
Fig. 16. Velocity fields in the vertical cross sections of the DEM particle assembly and particle velocity vectors behind and in front of the tool a) in the DEM-FEM simulation of the PMMA tool, b) in the DEM-FEM simulation of the S235 tool, c) in the DEM simulation of the S235 tool with 300 mm of tool displacement, at a 42 mm working depth (dimensions of the particle assembly in motion are given in mm and the direction of tool movement is indicated by vector **v**).

in front of the tool, while in the DEM simulation of the S235 tool, the particle velocities directly in front of the tool range from 23 to 28 mm s^{-1} (Fig. 16c). Therefore, it can be concluded that the velocity field is more heterogeneous when a passively vibrating PMMA tool is employed, compared to the more rigid S235 tool. It is also noticeable that in the DEM-FEM simulation of the PMMA tool, the depth of the particle assembly in motion is 83 mm (Fig. 16a), whereas in the DEM simulation of the S235 tool, it is 55 mm (Fig. 16b), and in the DEM simulation of the S235 tool, it is 58 mm (Fig. 16c). This indicates that with a passively vibrating PMMA tool, greater tillage depth and more substantial soil

loosening can be achieved at the same working depth compared to the more rigid S235 tool. However, it can also be observed that the width and length of the particle assembly in motion are smaller in the DEM-FEM simulation of the PMMA tool (Fig. 16a) than in the DEM-FEM and DEM simulations of the S235 tool (Fig. 16b and c). This can be explained by the more uniform velocity field which surrounded the S235 tool, with larger distances of transition between the particles moving at maximum velocity directly in front of the tool and the stationary particles. Furthermore, when comparing the velocity fields behind and in front of the tool, it can be seen that in the DEM simulation of the S235
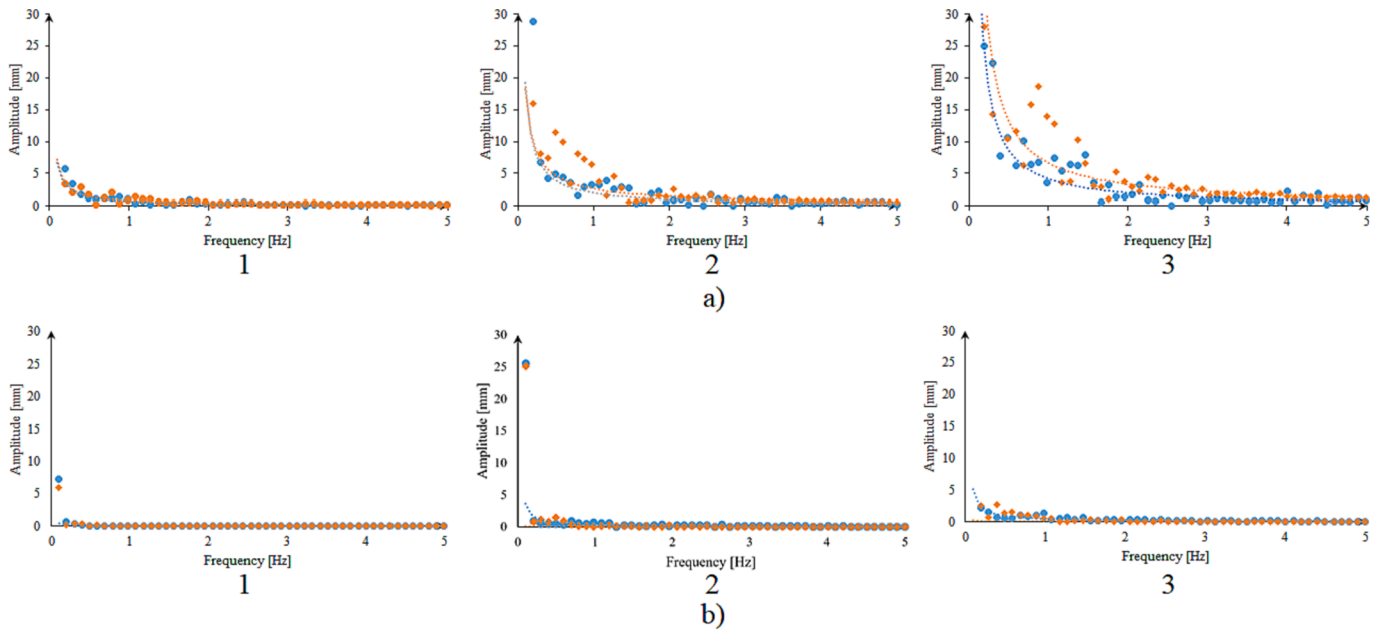
Fig. 17. Fast Fourier transformed ● (RGB 91, 155, 213) measured and ◆ (RGB 237, 125, 49) simulated deformation data of the coupled DEM-FEM simulations of the a) PMMA tool and b) S235 tool, and the fitted power curves on the ··· (RGB 91, 155, 213) measured and ··· (RGB 237, 125, 49) simulated data in 1: 18 mm, 2: 30 mm, 3: 42 mm working depth.

tool, the particle velocity vectors form more organized and longer streamlines (Fig. 16c), whereas in the DEM-FEM simulation of the PMMA tool, only shorter and more irregular streamlines are observed (Fig. 16a). This suggests that the use of passively vibrating tools results in a greater degree of soil mixing compared to rigid tools.

3.6. Fast Fourier Transform analysis results

The Fast Fourier Transformed (FFT) representation of the measured data and the FFT representation of the simulated data obtained from the coupled DEM-FEM simulations are shown in Fig. 17. It can be observed that both in the measurements and simulations, the amplitude of force and deformation generally decreases with increasing frequency. The PMMA tool exhibits larger amplitudes of vibration compared to the S235 tool, which can be attributed to its lower stiffness. Furthermore, it can be observed that increasing the working depth results in increased vibration amplitudes due to the higher forces present and the larger fluctuations in the forces. Power function curves were fitted on the FFT data using the least squares method, similarly to the procedure used in the study by Liang and Marshall (1990). Good agreement between the fitted power functions for the simulation and measurement data can be observed at 18 mm (Fig. 17a.1 and b.1) and at 30 mm (Fig. 17a.2 and b.2) working depths. However, at the 42 mm (Fig. 17a.3 and b.3) working depth, the power function fitted to the simulation data set exhibits higher amplitude compared to the power function fitted to the measurement data. This can be explained by the presence of higher amplitude vibrations at higher frequencies in the simulation. Therefore, it can be concluded that the FFT enabled the comparison of vibration parameters between measurements and simulations, allowing for further refinement of parameter calibration.

4. Conclusions

The main novelty value of the research is the development of a two-way coupled simulation procedure combining the discrete element method (DEM) and the finite element method (FEM), for the modelling of passively vibrating tillage tools, e.g., passively vibrating sweep tools, harrows and subsoilers. To validate the approach, simulations were

performed and empirical measurements were taken, and based on them the following conclusions can be drawn:

Soil properties are dependent on the depth of tillage, therefore a multi-layered soil model had to be created to accurately represent the varying properties of soil at different depths.

The FEM parameters can be calibrated using pure FEM simulations by measuring and simulating the dynamic response of the PMMA tool and the steady state deformation of the S235 tool under the load of different calibration weights.

The DEM parameters can be determined by performing pure DEM simulations using a highly rigid S235 tool and the hysteretic spring contact model supplemented by a linear cohesion secondary contact model.

The coupled DEM-FEM procedure developed for this study is applicable for calculating the mean draught force and deformation of passively vibrating soil tillage tools, as the coupled DEM-FEM simulations showed good agreement with the results from empirical measurements.

In the simulations, it was observed that the results were primarily influenced by the lowest soil layer that was in contact with the bottom of the soil-engaging tool, because this soil layer came into the most contact with the tool.

By comparing the coupled DEM-FEM simulation of the PMMA tool and the DEM simulation of the S235 tool, it could be observed that the passively vibrating PMMA tool influenced the motion of the particles at a greater depth, but over a shorter length and width in front of and to the side of the tool, and the velocities of the moving particles were less uniform compared to those obtained with the rigid S235 tool, which supports the assumption that passively vibrating tillage tools loosen and mix the soil more effectively and more inhomogenously around themselves than rigid tillage tools.

In both the simulations and the measurements, the Fast Fourier Transform (FFT) analysis proved to be an effective tool for analysing and comparing the characteristic frequencies of the forces acting on the soil-engaging tool and for investigating the characteristic frequencies of the deformation of the tool.

In order to achieve a more accurate match between the results of the simulations and the measurements, we suggest the application of

calibration procedures aided by artificial intelligence. Furthermore, as the study was carried out only in dry sandy soil, in order to better understand the interaction between passively vibrating tillage tools and the soil, different velocities, different soil types, different tool geometries and various tool materials could also be investigated, and the effect of soil moisture, state of compactness and texture could also be the focus of future studies.

CRediT authorship contribution statement

László Pásthy: Conceptualization, Formal analysis, Funding acquisition, Investigation, Methodology, Project administration, Software, Visualization, Writing – original draft. **Zsolt József Farkas:** Investigation, Resources. **Tamás Haba:** Software. **Kornél Tamás:** Conceptualization, Funding acquisition, Project administration, Resources, Supervision, Writing – review & editing.

Declaration of Competing Interest

The authors declare that they have no known competing financial interests or personal relationships that could have appeared to influence the work reported in this paper.

Data availability

Data will be made available on request.

Acknowledgement

Appendix A. Supplementary data

Supplementary data to this article can be found online at https://doi.org/10.1016/j.compag.2023.108459.

References

Abo-Elnor, M., Hamilton, R., Boyle, J.T., 2003. 3D Dynamic analysis of soil–tool interaction using the finite element method. J. Terramech. 40 (1), 51–62.

Asaf, Z., Rubinstein, D., Shmulevich, I., 2006. Evaluation of link-track performances using DEM. J. Terramech. 43 (2), 141–161.

Asuero, A.G., Sayago, A., González, A.G., 2006. The correlation coefficient: an overview. Crit. Rev. Anal. Chem. 36 (1), 41–59. https://doi.org/10.1080/10408340500526766.

Bahrami, M., Naderi-Boldaji, M., Ghanbarian, D., Ucgul, M., Keller, T., 2020. Simulation of plate sinkage in soil using discrete element modelling: calibration of model parameters and experimental validation. Soil Tillage Res. 203, 104700.

Bentaher, H., Ibrahmi, A., Hamza, E., Hbaieb, M., Kantchev, G., Maalej, A., Arnold, W., 2013. Finite element simulation of moldboard–soil interaction. Soil Tillage Res. 134, 11–16.

Budynas, R.G., Nisbett, J.K., 2011. Shigley's Mechanical Engineering Design. McGraw-Hill, New York.

Cho, S., 2018. Fourier Transform and Its Applications Using Microsoft EXCEL®. Morgan & Claypool Publishers.

Dongbao, Y., Junsong, G., Jianping, L., Chu, S., Shunying, J., 2021. Analysis of ice-inducted structure vibration of offshore wind turbines based on DEM-FEM coupled method. 力学学报 53 (3), 682–692.

Dratt, M., Katterfeld, A., 2017. Coupling of FEM and DEM simulations to consider dynamic deformations under particle load. Granul. Matter 19 (3), 49. https://doi.org/10.1007/s10035-017-0728-3.

Dzhabborov, N., Dobrinov, A., Sergeev, A., 2021. Vibration parameters and indicators of a dynamic tillage tool. IOP Conf. Ser.: Earth Environ. Sci. 937 (3), 032048.

Fenyvesi, L., Hudoba, Z., 2010. Vibrating tillage tools. In: Soil Engineering. Springer, pp. 31–49.

Gunn, J.T., Tramontini, V.N., 1955. Oscillation of tillage implements. Agri. Eng. 36 (11), 725–729.

Horváth, D., Tamás, K., Poos, T., 2022. Viscoelastic contact model development for the discrete element simulations of mixing process in agitated drum. Powder Technol. 397, 117038.

Huser, A., Kvernvold, O., 1998. Prediction of sand erosion in process and pipe components.

Keppler, I., Hudoba, Z., Oldal, I., Csatar, A., Fenyvesi, L., 2015. Discrete element modeling of vibrating tillage tools. Eng. Comput. 32 (2), 308–328. https://doi.org/10.1108/EC-10-2013-0257.

Kofoed, S.S., 1969. Kinematics and power requirement of oscillating tillage tools. J. Agric. Eng. Res. 14 (1), 54–73.

Liang, Z., Marshall, A.G., 1990. Time-domain (interferogram) and frequency-domain (absorption-mode and magnitude-mode) noise and precision in Fourier transform spectrometry. Appl. Spectrosc. 44 (5), 766–775.

Liberty, J., 2005. Programming C#: Building. NET Applications with C. O'Reilly Media Inc.

Mandel, J., 1990. Iterative solvers by substructuring for the p-version finite element method. Comput. Methods Appl. Mech. Eng. 80 (1–3), 117–128.

Michael, M., Vogel, F., Peters, B., 2015. DEM–FEM coupling simulations of the interactions between a tire tread and granular terrain. Comput. Methods Appl. Mech. Eng. 289, 227–248.

Naderi-Boldaji, M., Alimardani, R., Hemmat, A., Sharifi, A., Keyhani, A., Tekeste, M.Z., Keller, T., 2013. 3D finite element simulation of a single-tip horizontal penetrometer–soil interaction. Part I: development of the model and evaluation of the model parameters. Soil Tillage Res. 134, 153–162.

Nishiyama, K., Nakashima, H., Yoshida, T., Shimizu, H., Miyasaka, J., Ohdoi, K., 2018. FE-DEM with interchangeable modeling for off-road tire traction analysis. J. Terramech. 78, 15–25.

Programming Guide, n.d. Retrieved 10 April 2023, from https://2022.help.altair.com/2022.1/EDEM/Programming_Guide.htm.

Rao, G., Chaudhary, H., Sharma, A., 2018. Design and analysis of vibratory mechanism for tillage application. Open Agriculture 3 (1), 437–443.

Ridwan-Pramana, A., Marcian, P., Borak, L., Narra, N., Forouzanfar, T., Wolff, J., 2017. Finite element analysis of 6 large PMMA skull reconstructions: a multi-criteria evaluation approach. PLoS One 12 (6), e0179325.

Roessler, T., Richter, C., Katterfeld, A., Will, F., 2019. Development of a standard calibration procedure for the DEM parameters of cohesionless bulk materials–part I: solving the problem of ambiguous parameter combinations. Powder Technol. 343, 803–812.

Suhr, B., Six, K., 2017. Parametrisation of a DEM model for railway ballast under different load cases. Granul. Matter 19 (4), 64.

Szabó, D., Pásthy, L., Orosz, Á., Tamás, K., 2022. The investigation of additive manufacturing and moldable materials to produce railway ballast grain analogs. Frattura Ed Integrità Strutturale 16 (60), 213–228.

Tamás, K., 2018. The role of bond and damping in the discrete element model of soil-sweep interaction. Biosyst. Eng. 169, 57–70.

Tamás, K., Bernon, L., 2021. Role of particle shape and plant roots in the discrete element model of soil–sweep interaction. Biosyst. Eng. 211, 77–96.

Ucgul, M., Fielke, J.M., Saunders, C., 2015. Defining the effect of sweep tillage tool cutting edge geometry on tillage forces using 3D discrete element modelling. Inform. Process. Agricult. 2 (2), 130–141.

Ucgul, M., Saunders, C., Fielke, J.M., 2017. Discrete element modelling of tillage forces and soil movement of a one-third scale mouldboard plough. Biosyst. Eng. 155, 44–54.

Upadhyay, G., Raheman, H., 2020. Comparative assessment of energy requirement and tillage effectiveness of combined (active-passive) and conventional offset disc harrows. Biosyst. Eng. 198, 266–279.

Usaborisut, P., Sukcharoenvipharat, W., Choedkiatphon, S., 2020. Tilling tests of rotary tiller and power harrow after subsoiling. J. Saudi Soc. Agric. Sci. 19 (6), 391–400.

Van der Linde, J., 2007. Discrete Element Modeling of a Vibratory Subsoiler. University of Stellenbosch, Stellenbosch [PhD Thesis].

Wang, E.K., Jagfeld, M., 1993. Substructuring for large structures using finite element program ANSYS on a workstation. In: Control and Dynamic Systems, vol. 59. Elsevier, pp. 137–166.

Wang, Y., Jing, H., Zhang, D., Cui, T., Zhong, X., Yang, L., 2018. Development and performance evaluation of an electric-hydraulic control system for subsoiler with flexible tines. Comput. Electron. Agric. 151, 249–257.

Wang, D., Wang, Y., Yang, B.I.N., Zhang, W.E.I., Lancaster, N., 2008. Statistical analysis of sand grain/bed collision process recorded by high-speed digital camera. Sedimentology 55 (2), 461–470.

Wang, J., Yan, H., 2012. DEM analysis of energy dissipation in crushable soils. Soils Found. 52 (4), 644–657.

Wang, Y., Zhang, D., Yang, L., Cui, T., Zhang, W., Qi, B., Li, Y., Zhong, X., 2020. Field performance of an electric–hydraulic control system for vibrating subsoiler with flexible tines. Comput. Electron. Agric. 172, 105377.

Weng, S., Xia, Y., Xu, Y.-L., Zhu, H.-P., 2011. Substructure based approach to finite element model updating. Comput. Struct. 89 (9–10), 772–782.

Wu, S.R., 2006. Lumped mass matrix in explicit finite element method for transient dynamics of elasticity. Comput. Methods Appl. Mech. Eng. 195 (44–47), 5983–5994.

Yang, P., Zang, M., Zeng, H., 2020. DEM–FEM simulation of tire–sand interaction based on improved contact model. Comput. Particle Mech. 7 (4), 629–643.

Zeng, Z., Chen, Y., Zhang, X., 2017. Modelling the interaction of a deep tillage tool with heterogeneous soil. Comput. Electron. Agric. 143, 130–138.

Zeng, H., Xu, W., Zang, M., Yang, P., Guo, X., 2020. Calibration and validation of DEM-FEM model parameters using upscaled particles based on physical experiments and simulations. Adv. Powder Technol. 31 (9), 3947–3959.

Zhang, P., Yuan, J., Wang, D., Liu, X., Zheng, X., 2023. Development of a novel pull-cutting end-effector for ex-situ robotic harvesting of white asparagus based on MBD-DEM coupling simulation. Comput. Electron. Agric. 205, 107641.

Zhang, J., 1997. Vibratory Analysis of Tillage Operation [PhD Thesis, University of Saskatchewan]. https://harvest.usask.ca/handle/10388/etd-10212004-000546.

Zhong, H., Yu, Z., Zhang, C., Lyu, L., Zhao, L., 2022. Dynamic mechanical responses of reinforced concrete pier to debris avalanche impact based on the DEM-FEM coupled method. Int. J. Impact Eng 167, 104282.